Ternary ruthenium complex hydrides for ammonia synthesis

Qianru Wang[1,2]†, Jaysree Pan[3]†, Jianping Guo[1,4], Heine Anton Hansen[3], Hua Xie[1], Ling Jiang[1], Lei Hua[1], Haiyang Li[1], Yeqin Guan[1,2], Peikun Wang[1], Wenbo Gao[1,2], Lin Liu[1], Hujun Cao[1], Zhitao Xiong[1], Tejs Vegge[3]*, Ping Chen[1,4,5]*

[1]Dalian National Laboratory for Clean Energy, Dalian Institute of Chemical Physics, Chinese Academy of Sciences, Dalian, China.
[2]University of Chinese Academy of Sciences, Beijing, China.
[3]Department of Energy Conversion and Storage, Technical University of Denmark, 2800 Kgs. Lyngby, Denmark.
[4]Collaborative Innovation Center of Chemistry for Energy Materials, China.
[5]State Key Laboratory of Catalysis, Dalian, China.
*Correspondence to: teve@dtu.dk; pchen@dicp.ac.cn.
† These authors contributed equally to this work.

Ammonia is the feedstock for nitrogen fertilizers and a potential carbon-free energy carrier, but the current production emits more CO_2 than any other chemical producing reaction in the world. The demand for decarbonizing the ammonia industry by using renewable energy has renewed research interests into catalyst development for effective N_2 reduction under mild conditions – a grand scientific challenge. Conventional heterogeneous catalysts based on metallic Fe or Ru mediate dinitrogen dissociation and hydrogenation through a relatively energy-costing pathway. The ternary ruthenium complex hydrides Li_4RuH_6 and Ba_2RuH_6 reported in this work, on the other hand, represent an entirely new class of compound catalysts, which are composed of the electron- and H-rich [RuH_6] anionic centers for non-dissociative dinitrogen reduction, where hydridic H transports electron and proton between the centers, and the Li(Ba) cations for stabilizing N_xH_y (x: 0 to 2, y: 0 to 3) intermediates. The dynamic and synergistic involvement of all the components of the ternary complex hydrides facilitates a novel reaction mechanism with a narrow energy span and perfectly balanced kinetic barriers for the multi-step process, leading to ammonia production from N_2+H_2 with superior kinetics under mild conditions.

The energetics and mechanism of a catalytic process depend explicitly on the interaction between the reacting species and the active center, which is exemplified in the activation and conversion of N_2 to NH_3 over natural and man-made catalysts. In biological [1-2] or organometallic N_2 fixation [3-5] catalyzed by FeMo(V) cofactor or soluble transition metal (TM) complexes, N_2 coordinates to the ionic TM center in a mild exothermic manner and undergoes a hydrogen associative conversion, i.e., the reduction of the N≡N bond takes place synchronously with the formation of N-H bonds via successive or concerted proton and electron transfer steps. Despite operated under ambient conditions, these systems still consume a substantial amount of energy [6]. When the catalysis is carried out on an extended Fe or Ru metal surface, N_2 adsorbs on the active center composed of multiple TM atoms (C_7 or B_5 site of Fe or Ru, respectively) and dissociates exothermically into chemisorbed N atoms followed by a stepwise hydrogenation to NH_3 [7-10]. The relatively high kinetic barrier for direct N_2 dissociation and/or strong adsorption of intermediate species on Fe or Ru metal surface render NH_3 synthesis from N_2+H_2 under near-ambient conditions unattainable [11]. Creating an active center with suitable electronic structure and reacting environment for effective "hydrogenolysis" of N_2 to NH_3 by using H_2 as reductant would synergize the energy input and output in breaking and establishing chemical bonding, and thus

endow the catalysis of narrow energy span [12]. Encouraging attempts have been made via creating isolated or clustered TM center on an oxide support [13-14] , defect-borne Co_3Mo_3N surface [15], or new catalytic systems (such as electride/hydride-involved TM particle catalyst, intermetallic catalyst, etc.)[16-19], while catalytic hydrogenolysis of N_2 to NH_3 via concerted N-N weakening and N-H forming under mild conditions has yet to be demonstrated.

Recently, gas-phase cluster investigations revealed that laser-generated gaseous clusters such as $[Li_4FeH_6]^-$ and $[Li_5FeH_7]^-$ etc. from LiH-promoted Fe metal catalyst can undergo stoichiometric reaction with dinitrogen forming NH_2-containing clusters [20]. This finding inspired us to investigate whether the ternary complex hydrides of alkali (or alkaline earth) and transition metals, a series of compounds belonging to solid-state complexes that often studied in hydrogen storage [21], would have the potential to catalyze ammonia formation from N_2 and H_2. The synthesis of solid-state Li_4FeH_6 requires extremely high pressure of 6.1 GPa [22], but its Ru analogues are stable entities and can be facilely prepared under normal condition [23]. In this article, we report an entirely new catalyst system, i. e., ternary ruthenium complex hydrides Li_4RuH_6 and Ba_2RuH_6, for ammonia synthesis from N_2 and H_2. The ruthenium complex hydrides differ distinctly from the existing heterogeneous TM catalysts and homogeneous TM complex catalysts in electronic, compositional and structural properties as well as the reaction mechanism for ammonia synthesis, and exhibit remarkable catalytic performances under mild conditions, i.e., they outperform all the heterogeneous catalysts developed to date, and exhibit $N_2 + H_2$ to NH_3 activities at temperatures below 373 K! Through a concerted experimental and theoretical investigation, we demonstrate that catalytic hydrogenolysis of dinitrogen to ammonia could by effectively achieved by ruthenium complex hydrides under mild conditions, in which all the components of complex hydride, i. e., the electron-rich $[RuH_6]^{4-}$, Li/Ba cation and hydridic hydrogen, have a natural synergy during catalysis. These findings provide new insights into the catalyst design for mild-condition ammonia synthesis, and may also bridge the gap of heterogeneous and homogeneous nitrogen fixation at the molecular level.

Results

Structure and properties of ternary Ru complex hydrides. The ternary Ru complex hydrides are a class of mixed iono-covalent compounds having a general chemical formula of $A_x[RuH_6]$ (A = Li, Na, Mg, Ca or Ba etc., x= 4 or 2) [23-24]. Of particular interests are Li_4RuH_6 and Ba_2RuH_6, which can be synthesized via reacting Ru metal with LiH or BaH_2, respectively. Ru in Li_4RuH_6 has a low valence state as indicated by charge state analysis [24]. Our Bader charge calculations also reveal that Li donates electronic charge to $[RuH_6]$; H, on the contrary, is negatively charged (Supplementary Fig. 1). The H- and electron-rich $[RuH_6]^{4-}$ anions sit inside the K_4CdCl_6 (or K_2PtCl_6)-type framework of Li (or Ba) cations with a Ru-Ru distance of 5. 09 (5.78) Å (Supplementary Fig. 2). These ternary ruthenium complex hydrides differ distinctly from the closed packed Ru metal surface and the isolated molecular Ru complexes in electronic, compositional and structural properties as illustrated in Figs. 1a, 1b and 1c.

Our pressure-composition-isotherm and temperature-programmed reaction measurements reveal that Li_4RuH_6 has a large enthalpy change of 93.1 kJ mol^{-1}-H_2 in hydrogen desorption (the equilibrium H_2 desorption pressure is below 0.2 bar at 773 K), and only at high temperatures would Li_4RuH_6 decompose to Ru and LiH (Fig. 1d). Li_4RuH_6 is also resistant to diluted NH_3, i.e., upon feeding a mixture of NH_3 and H_2, the ternary complex hydride remains intact until ca. 673 K (Supplementary Fig. 3a). The *in situ* SR-PXD characterization also reveals that the hydride remains the dominant phase until ca. 651 or 738 K under N_2 or N_2+$3H_2$ of atmospheric pressure,

respectively (Fig. 1e and Supplementary Fig. 3b). Ba_2RuH_6 is found to be even more stable than Li_4RuH_6 (Supplementary Table 1 and Figs. 3c-d) [25]. These experimental results show that the bulk Li_4RuH_6 and Ba_2RuH_6 phases will remain stable under the ammonia synthesis conditions applied in this study (H_2 partial pressure from 0.25 to 7.5 bar, operation temperature from 323 K to 573 K).

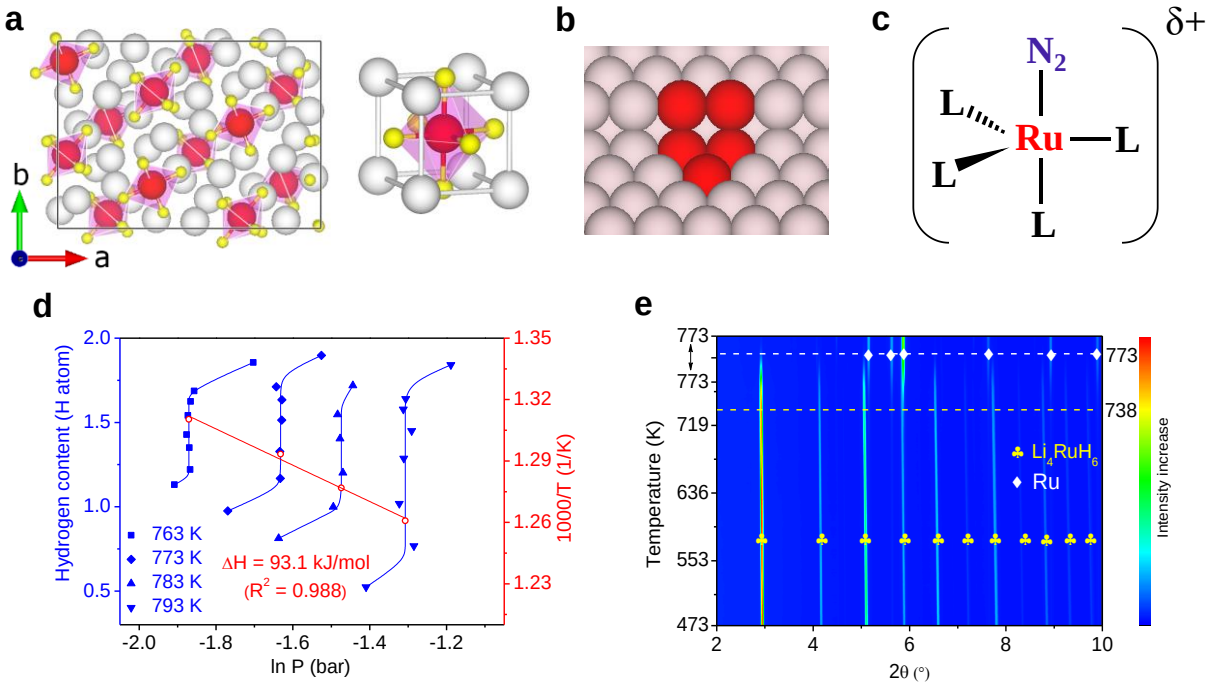

Fig. 1. Properties of Li_4RuH_6. a, Li_4RuH_6 surface with the unit cell of Li_4RuH_6 shown on the right side (Ru-red, H-yellow, Li-white). **b**, Ru (0001) surface (the B_5 site is highlighted in bright red). **c**, The model of molecular Ru complex (L-ligand). **d**, The pressure-composition isotherms of the dehydrogenation of Li_4RuH_6 and the corresponding van't Hoff plot, the lines are guide to eye. **e**, *in situ* SR-PXD characterization of Li_4RuH_6 sample under atmospheric N_2-$3H_2$ and elevated temperatures (from 473K to 773 K).

Catalytic performance and kinetic analyses. The as-prepared bulk-phase Li_4RuH_6 and Ba_2RuH_6 samples exhibit activities of ca. 150 and 120 μmol g_{cat}^{-1} h^{-1} at 1 bar and 573 K, respectively (Supplementary Fig. 4a). We then reduced the particle sizes of the samples to increase their surface areas. Our experimental results show that ball milling the as-prepared Li_4RuH_6 sample with inert dispersers, such as BN and MgO, can effectively reduce its crystalline size from ca. 50 nm to ca. 20 nm (Li_4RuH_6-BN(BM)) and 9 nm (Li_4RuH_6-MgO(BM)), and enhance the reaction rate by ca. 45 and 125 times, respectively (Fig. 2a). We thus employed MgO as support and synthesized Li_4RuH_6/MgO and Ba_2RuH_6/MgO catalysts by introducing Li and Ba to the parent Ru/MgO catalyst. These supported catalysts (their TEM images and HAADF-STEM characterizations are given in Supplementary Figs. 5-6) possess the characteristic features (Ru-H stretch and surface composition) of the bulk-phase hydrides (Supplementary Fig. 7). The Li_4RuH_6/MgO catalyst shows ca. 400-fold increase in activity from the bulk-phase Li_4RuH_6, but has a similar apparent activation energy of ca. 71 kJ mol^{-1} (0.74 eV) to other Li_4RuH_6-based catalysts (Fig. 2a and Supplementary Fig. 9a), manifesting an effective

exposure of active sites in the supported catalyst. The supported ternary complex hydride catalysts perform extraordinarily well under mild conditions and show constant activities for 100 hours (Figs. 2b and c). In particular, the Ba_2RuH_6/MgO significantly outperforms the most active Ru catalysts reported to date, and its activity at 523 K is over one order of magnitude higher than the benchmark Cs-promoted Ru/MgO catalyst (Table 1 and Supplementary Table 3). Moreover, under 10 bar and a WHSV of 7500 ml g^{-1} h^{-1}, the yield of ammonia is ca. 8.7 % at 573 K and approaches equilibrium at higher temperatures for the Ba_2RuH_6/MgO (Supplementary Fig. 8). Those features indicate the rich promise of the ternary complex hydrides for practical application in renewable electricity powered small-scale Haber-Bosch process, which generally requires an active catalyst operating at lower pressures (< 50 bar) and lower temperatures (< 673 K). It is important to note that if the Li_4RuH_6/MgO and Ba_2RuH_6/MgO samples are exposed to air, their activities drop significantly to the level of the Ru/MgO sample. Similarly, the direct introduction of Li_2O to Ru/MgO does not bring notable changes in activity (Supplementary Fig. 4b). This result demonstrates that the ternary complex hydride form is of critical importance for the efficient catalysis.

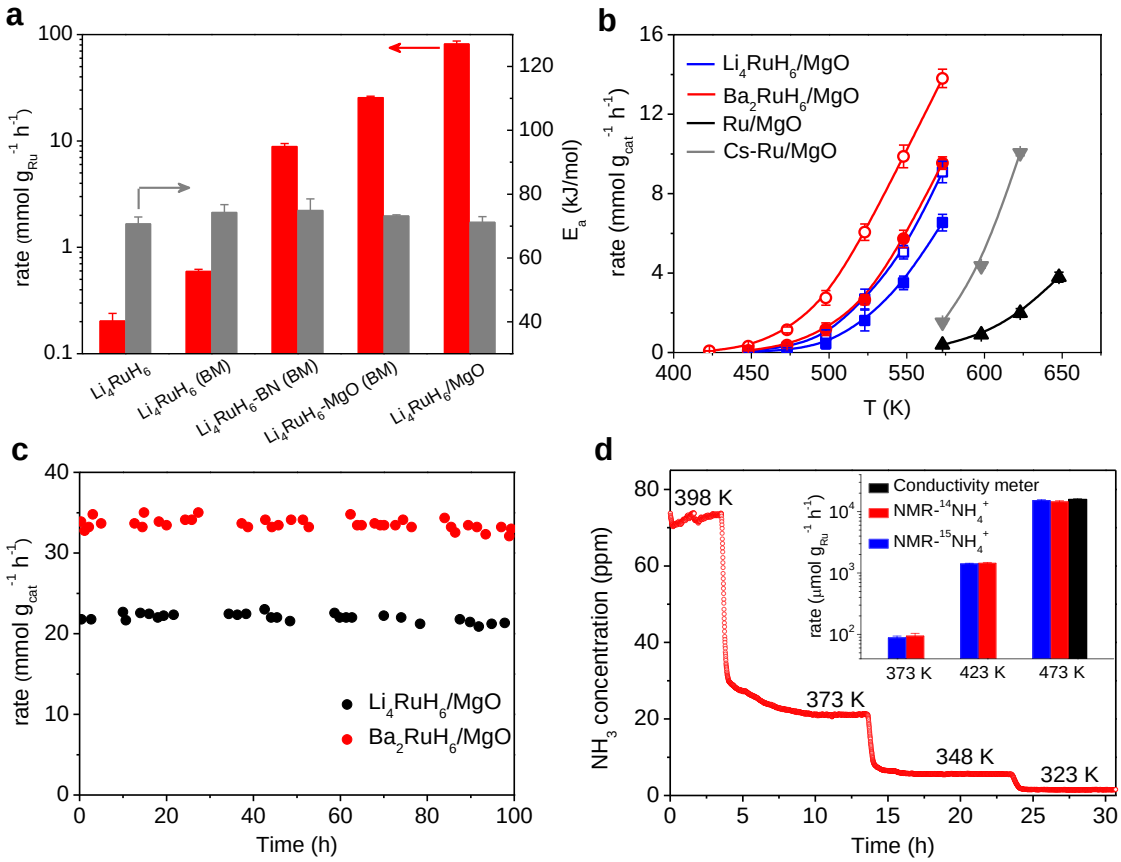

Fig. 2. Catalytic performances. a, Activities of Li_4RuH_6-based catalysts at 573 K and the corresponding activation energies (Reaction conditions: catalyst loading 30 mg, H_2:N_2=3:1, flow rate 30 ml min^{-1}, and 1 bar). **b**, Temperature-dependent NH_3 synthesis rates of different catalysts (Reaction conditions: H_2:N_2=3:1 (filled symbols) or H_2:N_2=2:3 (open symbols), others are the same as **a**). **c**, Time dependence of the activities of Li_4RuH_6/MgO and Ba_2RuH_6/MgO catalysts (Reaction conditions: H_2:N_2=2:3, 10 bar, others are the same as **a**). **d**, Time course of effluent

NH_3 concentration in the outlet gas (Ba_2RuH_6/MgO catalyst, 200 mg, H_2:N_2=1:3, flow rate 36 ml min^{-1}, 1 bar). The inset shows the activities of Ba_2RuH_6/MgO catalyst in the temperature range of 373-473 K determined by ^1H NMR measurements of NH_3 concentration in the outlet gas under a flow of $^{15}N_2$-H_2 or $^{14}N_2$-H_2. The activity at 473 K was also measured by conductivity meter for comparison. (30 mg, H_2:N_2=2:3, flow rate 10 ml min^{-1}, 1 bar). Error bars shown in **a**, **b** and inset figure of **d** represent the standard deviation from three independent measurements.

The most prominent kinetic features of this new class of ternary complex hydride catalysts are the smaller apparent activation energies and the positive reaction orders of H_2 (Table 1 and Supplementary Figs. 9b-e), which are distinctly different from other conventional Ru metal-based catalysts that suffer from severe hydrogen poisoning and thus exhibit strong temperature-activity dependence [10, 26]. These features enable the ternary complex hydride catalysts particularly effective at low temperatures, i.e., their operation temperatures are substantially down shifted by ca. 100 K from the pristine Ru/MgO (Fig. 2b). The Li_4RuH_6/MgO and Ba_2RuH_6/MgO catalysts present constant increases of turn-over-number (TON) at 448 K and 423 K, respectively, and the turn-on and turn-off NH_3 signals under an alternative feeding of N_2 + H_2 and H_2. Noted that no ammonia was detectable upon feeding N_2 only to Li_4RuH_6/MgO showing lattice H cannot work alone for ammonia (Supplementary Fig. 10). We subsequently probed the function limit of the hydride catalysts by adopting the charge-transfer ionization time-of-flight mass spectroscopy (CTI-TOFMS) with low NH_3 detection limit [27]. Under ambient pressure, both the CTI-TOFMS and the conductivity meter (the conventional ammonia detection method) gave similar effluent NH_3 concentrations of ca. 70 ppm at 398 K and 20 ppm at 373 K from the Ba_2RuH_6/MgO catalyzed system (Supplementary Fig. 11). The CTI-TOFMS further detected a constant effluent ammonia concentration of ca. 5 ppm at 348 K and 2 ppm at 323 K, respectively (Fig. 2d). In order to assert the origin of the nitrogen in the produced ammonia, we also performed a series of isotopic labeled control experiments and employed ^1H NMR for the quantitative measurements (Supplementary Fig. 12). As shown in Fig. 2d inset, feeding the Ba_2RuH_6/MgO catalyst with $^{15}N_2$-H_2 or $^{14}N_2$-H_2 results in nearly identical ammonia production rates, respectively, providing a conclusive evidence that the ammonia formed originates from the feeding gas.

Table 1. Catalytic Properties of Ru-based catalysts.

Catalyst	Ru content	r_{NH3}[a]		TOF[b]		Reaction order			E_a
	(wt %)	573 K	523 K	573 K	523 K	$\alpha(NH_3)$	$\beta(N_2)$	$\gamma(H_2)$	(kJ mol^{-1})
Li_4RuH_6/MgO	8.0	22.0	4.4	20.9	3.9	-0.59	0.91	0.30	71.2
Ba_2RuH_6/MgO	5.0	34.0	8.7	59.7	15.3	-0.63	0.92	1.00	63.9
Ru/MgO	8.7	1.7	0.25	1.3	0.2	-0.24	1.12	-0.86	94.8
Cs-Ru/MgO	7.3	5.7	0.60	9.9	1.1	-0.09	1.01	-0.82	112.4

[a] NH_3 synthesis rate (mmol g_{cat}^{-1} h^{-1}); catalyst loading 30 mg, H_2:N_2 =2:3, flow rate 30 ml min^{-1}, and 10 bar.

[b] TOF ($\times 10^{-3}$ s^{-1}) was calculated based on the surface Ru content derived from the average particle size observed by TEM and spherical assumption of the particle morphology (Supplementary Table 2). Conventional chemisorption measurement is not applicable to the ternary hydrides because they react with CO.

Reaction mechanism. Hydridic H is a combined source of electron and proton and was found to exert profound effects on nitrogen fixation [28]. In enzymatic ammonia synthesis catalyzed by FeMo- or FeV-cofactor, the key intermediate was suggested to be a bridging hydride species, which undergoes reductive elimination of dihydrogen to create an electron-enriched Fe center capable of catalyzing N_2 reduction [1-2]. Various manmade TM hydride complexes behave similarly and can serve as a platform for forming N_2 complexes [5, 29]. Some early TM hydrides such as multinuclear Ti hydride complex can further execute reductive protonation of N forming imido units [30-31]. Except that the highly reduced silyl functionalized $Fe(N_2)(H)_n$ complex undergoes unusual intramolecular hydride migration to N [32], no N-H bond formation was observed, however, over the reaction of N_2 and late TM hydride complexes owning to the insufficient activation of N_2 by electron-deficient TM center [5]. As a matter of fact, the Ru hydride complex $[PPh_3]_3Ru(H_2)H_2$ reacts with N_2 forming the dinitrogen complex $[PPh]_3Ru(N_2)H_2$ and H_2 [33]. As for heterogeneous Ru metal catalysts, the surface hydrides would exert a severe poisoning effect that defers low-temperature N_2 activation and conversion [26] and the H-associative mechanism is suppressed relative to the dissociative mechanism [34-35]. The H-rich ternary Ru complex hydrides, on the contrary, effectively catalyze N_2 and H_2 to NH_3 under mild conditions, reflecting a distinct electronic configuration and function mechanism of the active center.

We thus investigated the mechanism of ammonia formation over Li_4RuH_6 experimentally and theoretically (Fig. 3). The as-prepared Li_4RuH_6 sample was bombarded with laser to generate gaseous clusters for mass spectroscopy (MS) analysis. The composition and structure of the clusters would hint at or correlate with the surface of Li_4RuH_6 [20, 36]. Taking into the consideration of the isotopes of Ru, the clusters with relatively intensive peaks include $[Li_4RuH_6]^-$ and its complexes with LiH. Bombarding Li_4RuH_6 in N_2 atmosphere, interestingly, highlights the production of a set of NH_2-containing clusters (Fig. 3b).

Our DFT calculations show that the $[RuH_6]$ terminated (110) surface is the most stable low Miller index surface under operational conditions, and that the surface has an intriguing flexibility in accommodating excess lithium and hydrogen. As shown in Supplementary Fig. 13, the addition of excess LiH to the surface composed of six Li_4RuH_6 units is exothermic and results in the formation of $[RuH_7]$ complexes at the low-to-moderate temperatures and pressures investigated here. These data correlate with the observation of LiH affinity to $[Li_4RuH_6]^-$ in the cluster experiment (Fig. 3b). It is important to note that certain over-stoichiometry in surface hydrogen and lithium (two extra LiH) actually induces a preference for N_2 over H_2 adsorption at the active pentagonal base pyramidal polyhedral $[RuH_6]$ site. The competitive adsorption of N_2 and H_2 is not pronounced over Ba_2RuH_6, however, the addition of excess BaH_2 enhances N_2 adsorption, which may account for its higher TOF (see Supplementary Fig. 14 and Table 1). Based on the experimental observation and the theoretical calculations, a model Li_4RuH_6 (110) surface composed of six Li_4RuH_6 units and stabilized by two extra LiH was adopted to simulate NH_3 formation at 573 K and 1 bar.

The full reaction pathway has been mapped out using DFT calculations and found to be highly complex, involving no less than 13 intermediate states and multiple adsorption/dissociation and lattice H transfer processes. Given the complexity and dynamic nature of the surface, a large number of possible pathways were investigated (a few are shown in Supplementary Fig. 15), where the one shown in Fig. 3a was found to display the minimum energy span, i.e., the smallest free energy distance between the intermediate state and the transition state with the highest degree of rate control[12]. The energy span is as low as 1.75 eV under the mild experimental conditions

imposed here, which is substantially lower by >1.0 eV than that observed on Ru (211) [11], and in good agreement with the enhanced TOF observed relative to Ru/MgO (Table 1). Further, it is important to stress that although the path involves many activated processes, all of the kinetic barriers are found to below 79 kJ/mol (0.82 eV).

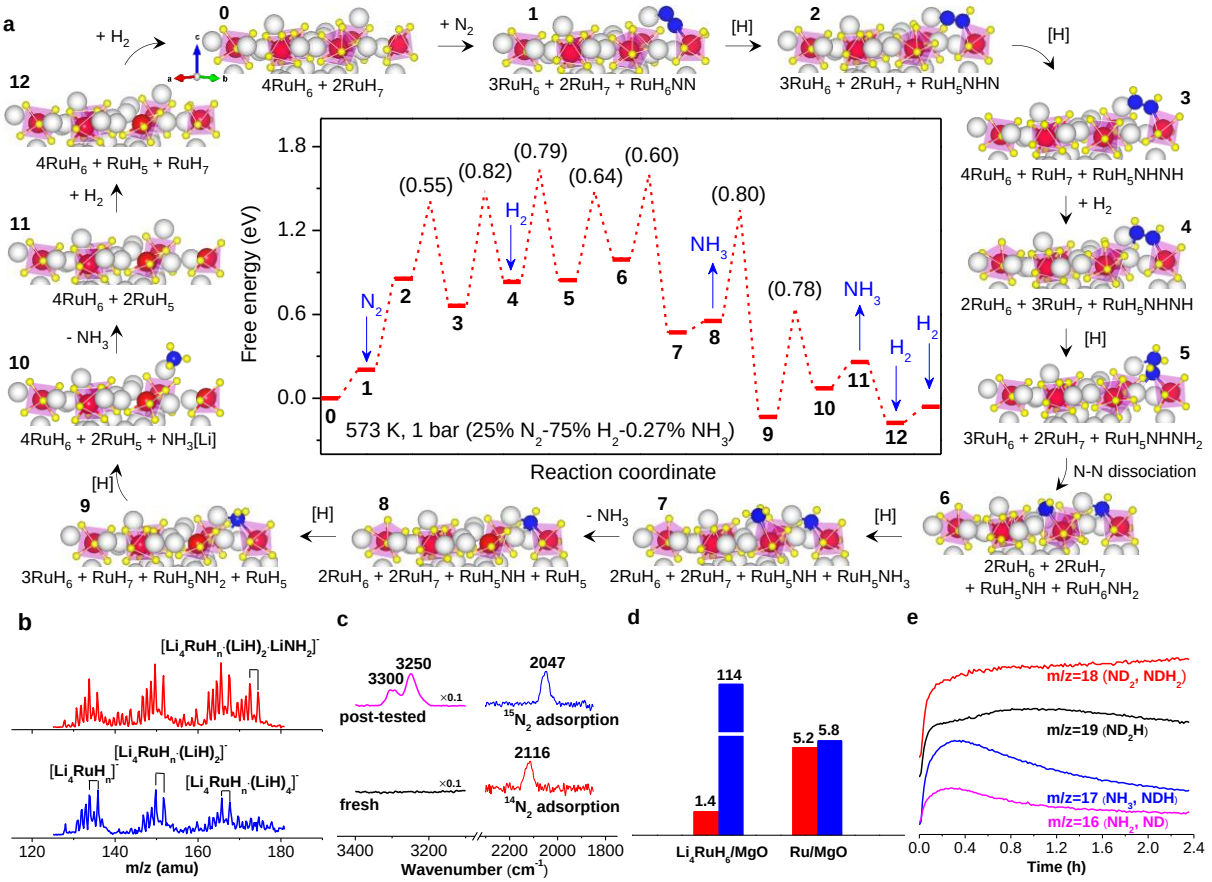

Fig. 3. Mechanistic investigations on N_2 activation and hydrogenation over Li_4RuH_6 surface. **a**, The calculated free energy pathway for the 13-step reaction mechanism with an energy span of only 1.75 eV, the kinetic barriers are enclosed in brackets. The images of the 13 states are simplified, [H] represents lattice hydrogen transfer. **b**, Mass spectra of clusters generated from Li_4RuH_6 sample under a pure He (blue line) and a mixture of N_2-He (red line) atmosphere. **c**, DRIFT spectra of the fresh, post-tested, and post-$^{14}N_2$ and -$^{15}N_2$ adsorbed Li_4RuH_6/MgO samples. **d**, The initial $^{28}N_2$-$^{30}N_2$ exchange rates (red bar) and catalytic NH_3 synthesis rates (blue bar) of Li_4RuH_6/MgO and Ru/MgO catalysts at 473 K (in μmol g_{cat}^{-1} h^{-1}). **e**, Reaction time profiles for ammonia synthesis from N_2 and D_2 over Li_4RuH_6 at 598 K.

Here, N_2 chemisorbs on the [RuH_6] site (**0**-**1**) in an end-on mode with an elongated N-N bond length of 1.14 Å manifesting a moderate activation, which correlates with our DRIFT observation of a N-N stretching of adsorbed N_2 at 2116 cm^{-1} (confirmed by $^{15}N_2$ adsorption at 2047 cm^{-1}) (Fig. 3c). The DFT calculations show that the direct dissociation of dinitrogen over the surface is strongly kinetically inhibited, which is understandable since Ru in Li_4RuH_6 is electron-deficient and the Ru-Ru distance (5.09Å) is much longer compared with that in Ru metal (2.71Å), which is unfavorable for the direct dissociation of dinitrogen. The non-dissociative N_2 activation is also supported by the of kinetic $^{15}N_2$-$^{14}N_2$ exchange experiments over Ru/MgO and Li_4RuH_6/MgO

samples, i. e., on the degassed Ru/MgO sample, the formation of $^{29}N_2$ with appropriate rate at 473 K was observed evidencing effective homolytic N_2 splitting on a Ru metal surface. However, such a phenomenon is not pronounced over the Li_4RuH_6/MgO sample, i.e., the initial $^{29}N_2$ formation rate is ca. 1/4 of that of Ru/MgO, in reverse order to their ammonia synthesis rates (Fig. 3d and Supplementary Fig. 16). A non-dissociative pathway is thus expected to prevail over Li_4RuH_6.

Our theoretical study shows that the hydrogenation of the adsorbed N_2 can happen both from the gaseous dihydrogen and from the lattice H, where the latter is preferred due to its lower kinetic barrier. In the full path presented by Fig. 3a, all the hydrogenation steps of the activated dinitrogen to form NH_3 take place only by lattice Hs, evidencing the role of lattice H in transporting electron and proton. While the gaseous dihydrogen molecule adsorption replenishes lattice H deficiency of the surface during the process. Such a mechanistic feature can be at least partially supported by the H/D isotope experiments, i.e., the H-rich ammonia and its fragments with m/z = 17 and 16 first increase and then decrease (Fig. 3e) when feeding the Li_4RuH_6 catalyst with N_2 and D_2.

As shown in Fig. 3, the first hydrogenation of the adsorbed N_2 (**1**-**2**) happens from the intra-site H (H from [RuH_6]-NN) and is endergonic by ca. 0.66 eV without kinetic barrier. The hydridic H is transferred to the polarized N-N antenna and undergoes reductive protonation forming activated [RuH_5]-NHN species, where both N atoms gain electrons from the hydridic H and bond with neighboring Li (Li-N bond length is 1.90 Å) (The Bader charge analyses are given in Supplementary Fig. 17). The second ([RuH_5]-NHNH) and the third ([RuH_5]-$NHNH_2$) hydrogenation steps (**2**-**3** and **4**-**5**) occur by the reductive protonation of the lattice Hs transferred from the neighboring [RuH_7] sites and assist by surface Li (Supplementary Fig. 18a). The N-N bond dissociates via a Li-assisted multi-step path with a kinetic barrier of 0.64 eV creating a [RuH_5]-NH and a [RuH_6]-NH_2 species (**5**-**6**) (Supplementary Fig. 18b). The first NH_3 ([RuH_5]-NH_3) formed from the intra-site H transfer (**6**-**7**) desorbs from the surface without kinetic barrier (**7**-**8**). The remaining [RuH_5]-NH species then consumes two lattice Hs from two neighboring [RuH_7] sites and forms [RuH_5]-NH_2 (**8**-**9**) and the second NH_3 species (**9**-**10**), respectively (Supplementary Fig. 18c). The second NH_3 species leaves Ru and hangs loosely on the neighboring Li (as [Li]-NH_3) and then desorbs from the surface (**10**-**11**). The surface is then replenished by the second and the third dihydrogen adsorption and restores the initial state (**11**-**12** and **12**-**0**).

It is important to note that every N_xH_y species formed as well as the transition state between every step during the process shows strong interaction with the neighboring Li ions on the surface (Li-N bond length in-between 1.90-2.00 Å), i. e., Li cation stabilizes the N_xH_y species and helps reducing the kinetic barriers, which shares some common features with that of N-K bond formation in molecular Fe and U nitride complexes during nitrogen reduction and functionalization, and that of Li-N bond formation in the Li-mediated electrochemical ammonia synthesis [37-39]. Also noted is that the most stable intermediate predicted is the Li-stabilized [RuH_5]-NH_2, which correlates well with the DRIFT observation of a pair of broad N-H stretches centered at ca. 3300 and 3250 cm^{-1} of the catalyst sample quenched from reaction (Fig. 3c) and the identification of NH_2-containing clusters in the cluster reaction (Fig. 3b). This mechanism results in positive reaction orders with respect to H_2 and N_2 and negative order of NH_3, agreeing well with our experimental findings and clearly distinguishing it from existing metallic ruthenium-based catalysts (Table 1).

Conclusions

The ternary ruthenium complex hydride may serve as the very first example of TM complex compound that can catalyze ammonia formation from dihydrogen and dinitrogen. The non-dissociative N_2 reduction is realized effectively by the cooperation of multiple electron-rich [$RuH_{5/6/7}$] sites, the involvement of lattice hydridic H as proton and electron carrier, and the role of alkali/alkaline earth metal cation in stabilizing N_xH_y intermediate species. The dynamic and synergistic engagement of all the active components of ternary hydride in the catalysis demonstrates the increased freedom and power in manipulating the energetics of the elementary steps and thus opens an avenue for the design and development of efficient catalyst tackling the conversion of kinetically stable molecules.

Methods

All the materials handlings were performed in a glove box filled with purified argon to keep a low water vapor concentration (< 0.1 ppm) and a low oxygen concentration (< 1 ppm). N_2 (99.999%), H_2 (99.9999%), D_2 (99.999%), Ar (99.999%), N_2/H_2 mixture with different molar ratios (99.9999%) were purchased from Dalian Special Gases Co., LTD.

Preparation of Li_4RuH_6 (Li_4RuD_6) and Ba_2RuH_6 samples. Both Li_4RuH_6 (Li_4RuD_6) and Ba_2RuH_6 were synthesized by the calcination of ball-milled mixtures of LiH (LiD) (LiH: Alfa, 99.4% metals basis; LiD: Aldrich, 98 atom% D) or BaH_2 with Ru powder (Aladdin, 99.9% metals basis) in hydrogen (deuterium) at elevated temperatures and pressures, as has been described in earlier reports [40-41]. BaH_2 was obtained following the procedure described previously [42]. The crystalline sizes of the as-prepared Li_4RuH_6 and Ba_2RuH_6 were estimated to be ca. 50 and 65 nm, respectively, by using the Scherrer equation based on the collected PXRD patterns.

Preparation of ball milled catalyst samples. Li_4RuH_6 was ball milled in a H_2-filled vessel on a Retsch planetary ball mill (PM 400, Germany) at 150 r.p.m for 3h, and was denoted as Li_4RuH_6 (BM). Li_4RuH_6-BN (BM) or Li_4RuH_6-MgO (BM) was prepared via ball milling Li_4RuH_6 and BN (Aladdin, 99.9% metals basis, 1~2 μm) or MgO powder under the same conditions as that of Li_4RuH_6 (BM), in which the Ru content is ca. 8 wt %. The MgO sample has a high specific surface area of ca. 534 $m^2 g^{-1}$, which was synthesized according to the literature report [43]. The crystalline sizes of Li_4RuH_6-BN (BM) and Li_4RuH_6-MgO (BM) were estimated to be ca. 20 and 9 nm, respectively, by using the Scherrer equation based on the collected PXRD patterns.

Preparation of Ru/MgO catalyst. Ru metal was deposited on the MgO support according to a urea-based decomposition precipitation (DP) method as reported in literature [44-45]. The sample was further reduced in pure H_2 at 673 K for 5 h and was denoted as the Ru/MgO. The Ru content of as-prepared Ru/MgO catalyst was determined to be 8.7 wt % by inductively coupled plasma mass spectrometry (ICP-AES, PerkinElmer ICP-AES 7300DV). The average Ru particle size of as-prepared Ru/MgO is ca. 3.09 nm (Supplementary Fig. 5).

Preparation of Li_4RuH_6/MgO and Ba_2RuH_6/MgO catalysts. Li_4RuH_6/MgO catalyst with a Ru loading of ca. 8.0 wt % was prepared as follows. The reduced Ru/MgO was impregnated in a lithium-ammonia solution with a molar ratio of Li:Ru=4:1, where Li metal (Macklin, 99.9% metals basis) can be easily converted to $LiNH_2$ in the presence of Ru. After evacuating the excess NH_3, the obtained sample was subsequently treated under 1 bar of H_2 at 573 K until no ammonia is detectable by the conductivity meter (Mettler Toledo SevenMulti), thus enabling *in situ* formation of Li_4RuH_6 on MgO support according to the following reaction:

$$4LiNH_2 + Ru + 5H_2 \rightarrow Li_4RuH_6 + 4NH_3$$

The Ba_2RuH_6/MgO catalyst with a Ru content of 5.0 wt % was prepared in a similar way, except impregnating the Ru/MgO in a barium-ammonia solution.

Preparation of Li_4RuH_6/MgO-air and Ba_2RuH_6/MgO-air catalysts. The obtained supported ternary Ru hydrides were exposed to air for 2 days for sufficient oxidation, then underwent *in situ* reduction by H_2–N_2 before catalytic testing. The obtained samples were referred as Li_4RuH_6/MgO-air and Ba_2RuH_6/MgO-air, respectively.

Preparation of Li_2O-Ru/MgO and Cs-Ru/MgO catalysts. The Li_2O-Ru/MgO and Cs-Ru/MgO catalysts were obtained by impregnating Ru/MgO with solutions of $LiNO_3$ (Kermel, ≥ 99.0%) and $CsNO_3$ (Guangfu, ≥99.0%) followed by H_2 reduction at 673 K for 5 h. The Li or Cs to Ru molar ratio is 4:1 or 1:1, respectively. The Ru content of Cs-Ru/MgO catalyst was determined to be 7.3 wt %.

Catalytic reaction tests. Ammonia synthesis was conducted in a stainless steel fixed-bed reactor with a quartz liner that operated with the supply of continuous-flow of extra pure N_2-H_2 mixture gas (>99.9999%). Typically, 30 mg of catalyst was loaded in the liner tube on a bed of quartz wool and subsequently heated at a ramping

rate of 5 K min^{-1} under the given pressure and flow rate. The ammonia produced was trapped in a diluted sulfuric acid solution and the proton conductivity was recorded with time by a conductivity meter. The principle of the NH_3 quantification method has been described previously [46]. The activity data at each temperature was monitored when the catalytic performance reached a steady-state value. Blank test using the same setup did not give any measurable activity at temperatures below 673 K and 10 bar.

TEM and STEM-EDS measurement. Transmission electron microscopy (TEM) images were recorded on a JEM-2100 microscope, operating at an accelerating voltage of 200 kV. More than 100 particles were measured from TEM images to determine the average particle size and particle size distributions. The compositions of the catalyst, including spectral imaging to produce elemental maps were captured using high angle annular dark field scanning transmission electron microscopy (HAADF-STEM, JEM-2100F) equipped with an energy dispersive X-ray spectroscopy (EDS) detector.

FTIR measurement. Fourier transform infrared measurements were conducted on a Brucker Tensor II unit in the diffuse reflection (DRIFT) mode with a scan resolution of 4 cm^{-1} and an accumulation of 32 scans each time.

N_2 physisorption. The Brunauer-Emmet-Teller (BET) specific surface areas of the samples were determined from nitrogen adsorption-desorption isotherms measured at 77 K using an automatic gas adsorption instrument (QUADRASORB SI).

Powder X-ray diffraction (PXRD) measurement. PXRD patterns were collected on a PANalytical X'pert diffractometer equipped with Cu Kα radiation (40 KV, 40 mA) for phase identification. The test samples were loaded in a homemade sample cell that was covered with KAPTON film to avoid air or moisture contamination.

***In situ* synchrotron radiation powder X-ray diffraction (SR-PXD) measurement.** *In situ* SR-PXD experiments were performed at the diffraction beamline P.02.1, DESY (Hamburg, Germany). The *in situ* cell and the procedure used were described elsewhere [47]. The wavelength was fixed at ca. 0.207 Å and a PerkinElmer XRD1621 plate image detector (2048*2048 pixel, each of size 200*200 microns) was used to acquire the patterns, with a sample-to-detector distance of about 1400 mm. The sample was loaded in a sapphire capillary tube (0.8 mm ID) and placed in a home-made sample holder. The Li_4RuH_6 sample was heated from 298 to 773 K with a ramping rate of 1 K min^{-1} in a stream of flow gas (10 ml min^{-1}). The Ba_2RuH_6 sample was heated from 298 to 923 K with a ramping rate of 6 K min^{-1} in a steam of flow gas (5 ml min^{-1}). The 2D images were then integrated using FIT2D software.

Temperature programmed techniques. Temperature-programmed desorption (TPD) measurements were conducted in a quartz-lined stainless steel reactor and the exhaust gases were monitored with an on-line mass spectrometer (MS, Hiden HPR20). Samples (30 mg) were heated in a stream of Ar (30 ml min^{-1}) from room temperature to desired temperatures at a ramping rate of 5 K min^{-1}. Temperature-programmed reaction (TPR) with specific gas was performed with the same apparatus and similar procedures as used in TPD, except the change of carrier gas.

Pressure-composition-temperature (PCT) measurement. PCT dehydrogenation experiments were carried out on a gas reaction controller (Advanced Materials Corporation, USA) loaded with 800 mg of Li_4RuH_6 sample. Static P-C isotherms were determined at temperatures of 763 K, 773 K, 783 K and 793 K, respectively. The control precision of the sample temperature was ±1 K. The initial pressure in the sample chamber for hydrogen desorption was ca. 1 bar.

Monitoring of catalytic synthesis of NH_3 by vacuum ultraviolet (VUV)-lamp-based charge-transfer ionization time-of-flight mass spectroscopy (CTI-TOFMS). Real-time monitoring of ammonia synthesis at low temperatures was realized by building an integrated apparatus that consists of the home-built NH_3 synthesis setup (described above) and the time-of-flight mass spectroscopy equipped with VUV-lamp-based

CTI-TOFMS. Full details of the VUV-lamp-based CTI-TOFMS were described in previous reports [27, 48]. To calibrate the instrument response (i.e., peak area) with respect to analyte concentration, ammonia standard gas mixture with concentration of 100 ppmv in syngas (H_2:N_2=1:3) was diluted with NH_3-free syngas (H_2:N_2=1:3) to a series of lower concentrations. Supplementary Fig. 11a shows the calibration curve of the NH_3^+ ions, and the dynamic range was obtained from 2 ppm to 100 ppm with a good linear correlation coefficient (R^2=0.996). 200 mg of catalyst was loaded and tested under a flow of syngas (H_2:N_2=1:3, 36 ml min^{-1}). The reaction temperature was varied from 398 K to 323 K and the pressure was kept at 1 bar. The signals of NH_3^+ (17 amu), H_2O^+ (18 amu), H_3O^+ (19 amu) and O_2^+ (32 amu) ions were recorded during the catalytic process. The background signal of NH_3^+ ion, determined in the same setup but without catalyst loading, was also detected as the baseline.

Gas-phase optical spectroscopy coupled with mass spectroscopy (GOS-MS) experiment. GOS-MS experiment was carried out using a homemade instrument with a laser vaporization source and a dual-channel time-of-flight mass spectrometer (D-TOFMS). Details of the apparatus has been described elsewhere [49], and only a brief outline of the experiment is given below. The species were generated via pulsed laser vaporization cluster source using the second harmonic of a Nd:YAG laser (Contimuum Minilite II). The sample was ablated in the presence of a supersonic beam of carrier gas. The typical stagnation pressure of carrier gas was about 3-5 bar. Under the efficient cooling by supersonic expansion of pulsed carrier gas, the clusters were cooled to ~200 K in the vacuum chamber and reacted with the pulsed gaseous reactants. The cluster ions were analyzed by the TOF mass spectrometer. Bombarding the surface of Li_4RuH_6 sample in pure He atmosphere gives a series of mass peaks. Taking account the contribution of various Ru isotopes [50], the relatively intense peaks at m/z=134, 136, 150, 152, 166 and 168 amu can be assigned to $[Li_4RuH_4]^-$, $[Li_4RuH_6]^-$, $[Li_4RuH_4{\cdot}(LiH)_2]^-$, $[Li_4RuH_6{\cdot}(LiH)_2]^-$, $[Li_4RuH_4{\cdot}(LiH)_4]^-$ and $[Li_4RuH_6{\cdot}(LiH)_4]^-$ clusters, respectively. A set of $LiNH_2$-containing clusters were observed from the Li_4RuH_6 sample bombarded in a mixture of N_2-He (1:9), which are assigned to the $[Li_4RuH_4{\cdot}(LiH)_2{\cdot}LiNH_2]^-$ (m/z=173 amu) and $[Li_4RuH_6{\cdot}(LiH)_2{\cdot}LiNH_2]^-$ (m/z=175 amu) clusters, respectively.

N_2 isotope labeling experiment. The identification and quantification of small amount of produced NH_3 at lower temperatures should be careful [51]. To verify the origin of NH_3 from N_2 at lower temperatures, isotopic labeling experiment was carried out using a mixture of $^{15}N_2$ (≥98%, Cambridge Isotope Laboratories, Inc.) and H_2 as the feeding gas (H_2:$^{15}N_2$=2:3). We employed ^1H NMR to measure ammonia production rates from $^{14}N_2$-H_2 and $^{15}N_2$-H_2 following the procedure described in literature [52-53], where $^{14}NH_4^+$ and $^{15}NH_4^+$ can be distinguished by the ^1H spectra in which coupling to ^{14}N is a triplet and coupling to ^{15}N is a doublet. The $^{15}NH_3$ or $^{14}NH_3$ produced was trapped in a diluted sulfuric acid solution (pH≈3) and quantified by using ^1H NMR spectroscopy. For the NMR studies, the pH of the solutions to be tested was adjusted to 2 using concentrated hydrochloric acid aqueous solution. 5 vol% DMSO-d_6 (99.9 atom % D, 0.03% (v/v) TMS) was added for deuterium locking and referencing. All NMR experiments were performed at 298 K on a Bruker Advance III spectrometer operating at a ^1H frequency of 500 MHz. A total of 1000 transient scans were accumulated for each sample. Calibration samples were prepared with varying concentrations of $^{14}NH_4Cl$ (Aladdin, 99.999%) and $^{15}NH_4Cl$ (Aladdin, 99 atom%).

H/D isotope experiment. Ammonia synthesis from N_2 and D_2 over the Li_4RuH_6 sample was conducted using a quartz-lined stainless steel reactor connected to a home-made device that can switch instantly between two gas streams under the same temperature and pressure. Prior to isotopic reaction, the sample (ca. 30 mg) was heated to 598 K and kept for a while under atmospheric Ar flow (30 ml min^{-1}). The mixture of N_2-D_2 (1:3, 30 ml min^{-1}) was subsequently switched to the sample and the effluent gas was analyzed with a mass spectrometer (MS, Hiden HPR20). The m/z=2, 3, 4, 15, 16, 17, 18, 19 and 20 masses were recorded as a function of time to follow the reaction. ND_3 (m/z=20 amu) was hardly differentiated due to an overlap with the fragment of Ar (m/z=20 amu).

N_2 isotopic exchange experiment. N_2 isotopic exchange reactions were performed using a home-made stainless steel reactor connected with vacuum-pumping system. The sample was loaded into the reactor in an Ar-filled glovebox and the loading amount is 30 mg for Ru/MgO or Li_4RuH_6/MgO and 225 mg for the

bulk-phase Li_4RuH_6. Prior to the exchange reactions, the Ru/MgO sample was degassed at 673 K and held for 2 h under vacuum. Li_4RuH_6/MgO and bulk-phase Li_4RuH_6 samples were treated in vacuum at 473K. A mixture of $^{15}N_2$ and $^{14}N_2$ ($^{15}N_2$:$^{14}N_2$=1:4.4, total pressure: ca. 0.55 bar) was then introduced to the samples at 473 K for the exchange reaction. The m/z=28, 29, 30 masses were monitored as a function of time to follow the reaction by using a mass spectrometer.

Kinetic studies. The measurements of reaction order of N_2 or H_2 were carried out with a flow of mixed gas (N_2, H_2 and Ar) under conditions (573 K, 1 bar, WHSV=60000 ml g^{-1} h^{-1}), where the effluent NH_3 concentration was kept constant. Our measurement conditions were far from equilibrium considering that the thermodynamic limit is ca. 2.1% under these conditions. The loading amount is 30 mg for Li_4RuH_6/MgO, Ba_2RuH_6/MgO and Cs-Ru/MgO, and 50 mg for Ru/MgO. The gas compositions of N_2:H_2:Ar were 5:50:45, 15:50:35, 25:50:25, 35:50:15, 45:50:5 for determining the N_2 order, and 20:40:40, 20:50:30, 20:60:20, 20:70:10, 20:80 for determining the H_2 order, respectively. The NH_3 order was determined by changing the flow rate of syngas while keeping a constant N_2 to H_2 partial pressure. Apparent activation energies were measured under atmospheric syngas (H_2:N_2=3) with a flow rate of 30 ml min^{-1}. The temperature range is 523-598 K for Li_4RuH_6/MgO (30 mg), 523-573 K for Ba_2RuH_6/MgO (30 mg), 573-648 K for Ru/MgO (30 mg) and 573-623 K for Cs-Ru/MgO (30 mg), respectively.

Theoretical calculations. For all theoretical calculations in this report we used density functional theory (DFT) with generalized gradient approximation (GGA) for the exchange-correlation potential, a plane-wave basis set and the projector augmented wave (PAW) method [54-55] as implemented in the Vienna ab-initio simulation package (VASP) [56]. In this study, we set a 500 eV energy cut-off for the plane-wave basis. The free energies were calculated with ideal gas limit approximation [57] and harmonic limit/hindered harmonic limit approximation [58-60] for the gaseous molecules and for the absorbates respectively. For simulating hydrogen gas in vacuum, we used a negligible partial pressure of 10^{-9} Pa. The kinetic pathways and their corresponding barriers presented here were determined by the nudge elastic band method (NEB) [61] implemented in VASP. To study the Li_4RuH_6 surface, we created slabs containing four layers of the material in the (110) direction (with regards to the primitive Li_4RuH_6 cell) and with six Ru-sites on the surface. We imposed 18 Å vacuum above the top layer of the slabs to avoid the interaction between the periodic images. During every simulation, the ions in the bottom two layers of these slabs remained fixed.

References

1. Hoffman, B. M., Lukoyanov, D., Dean, D. R. & Seefeldt, L. C. Nitrogenase: a draft mechanism. *Acc. Chem. Res.* **46**, 587-595 (2013).
2. Sippel, D. *et al.* A bound reaction intermediate sheds light on the mechanism of nitrogenase. *Science* **359**, 1484-1489 (2018).
3. Yandulov, D. V. & Schrock, R. R. Catalytic reduction of dinitrogen to ammonia at a single molybdenum center. *Science* **301**, 76-78 (2003).
4. Ashida, Y., Arashiba, K., Nakajima, K. & Nishibayashi, Y. Molybdenum-catalysed ammonia production with samarium diiodide and alcohols or water. *Nature* **568**, 536-540 (2019).
5. Nishibayashi, Y. *Nitrogen fixation (Topics in Organometallic Chemistry)* 1st edn, Vol. 60 (Springer, Heidelberg, 2017).
6. van der Ham, C.J. M., Koper, M. T. M., Hetterschied, D. G. H. Challenges in reduction of dinitrogen by proton and electron transfer. *Chem. Soc. Rev.* **43**, 5183-5191 (2014).
7. Jennings, J. R. *Catalytic ammonia synthesis: fundamentals and practice* 1st edn (Spinger, New York, 1991).
8. Dahl, S., Törnqvist, E. & Chorkendorff, I. Dissociative adsorption of N_2 on Ru(0001): A surface reaction totally dominated by steps. *J. Catal.* **192**, 381-390 (2000).
9. Honkala, K. *et al.* Ammonia synthesis from first-principles calculations. *Science* **307**, 555-558 (2005).
10. Aika, K.-i. Role of alkali promoter in ammonia synthesis over ruthenium catalysts—Effect on reaction mechanism. *Catal. Today* **286**, 14-20 (2017).
11. Vojvodic, A. *et al.* Exploring the limits: A low-pressure, low-temperature Haber–Bosch process. *Chem. Phys. Lett.* **598**, 108-112 (2014).

12. Kozuch, S. & Shaik, S. How to conceptualize catalytic cycles? The energetic span model. *Acc. Chem. Res.* **44**, 101-110 (2011).
13. Avenier, P. *et al.* Dinitrogen dissociation on an isolated surface tantalum atom. *Science* **317**, 1056-1060 (2007).
14. Liu, J.-C. *et al.* Heterogeneous Fe_3 single-cluster catalyst for ammonia synthesis via an associative mechanism. *Nature Commun.* **9**, 1610 (2018).
15. Zeinalipour-Yazdi, C. D., Hargreaves, J. S. J. & Catlow, C. R. A. Low-T mechanisms of ammonia synthesis on Co_3Mo_3N. *J. Phys. Chem. C* **122**, 6078-6082 (2018).
16. Kitano, M. *et al.* Ammonia synthesis using a stable electride as an electron donor and reversible hydrogen storage. *Nat. Chem.* **4**, 934-940 (2012).
17. Wang, P. *et al.* Breaking scaling relations to achieve low-temperature ammonia synthesis through LiH-mediated nitrogen transfer and hydrogenation. *Nat. Chem.* **9**, 64-70 (2017).
18. Gong, Y. *et al.* Ternary intermetallic LaCoSi as a catalyst for N_2 activation. *Nat. Catal.* **1**, 178-185, (2018).
19. Tang, Y. *et al.* Metal-dependent support effects of oxyhydride-supported Ru, Fe, Co catalysts for ammonia synthesis. *Adv. Energy Mater.* **8**, 1801772 (2018).
20. Wang, P. *et al.* The formation of surface lithium–iron ternary hydride and its function on catalytic ammonia synthesis at low temperatures. *Angew. Chem. Int. Ed.* **56**, 8716-8720 (2017).
21. K. Yvon, G. Renaudin, Hydrides: solid state transition metal complexes, John Wiley & Sons Ltd, (2006).
22. Saitoh. H. *et al.* Li_4FeH_6: iron-containing complex hydride with high gravimetric hydrogen density. *APL Mater.* **2**, 076103 (2014).
23. Humphries, T. D., Sheppard, D. A. & Buckley, C. E. Recent advances in the 18-electron complex transition metal hydrides of Ni, Fe, Co and Ru. *Coord. Chem. Rev.* **342**, 19-33 (2017).
24. Orgaz, E. & Aburto, A. Electronic structure of ternary ruthenium-based hydrides. *J. Phys. Chem. C* **112**, 15586-15594 (2008).
25. Nicholson, K. M. & Sholl, D. S. First-principles screening of complex transition metal hydrides for high temperature applications. *Inorg. Chem.* **53**, 11833-11848 (2014).
26. Rosowski, F. *et al.* Ruthenium catalysts for ammonia synthesis at high pressures: Preparation, characterization, and power-law kinetics. *Appl. Catal. A-Gen.* **151**, 443-460 (1997).
27. Xie, Y. *et al.* Long-term real-time monitoring catalytic synthesis of ammonia in a microreactor by VUV-lamp-based charge-transfer ionization time-of-flight mass spectrometry. *Anal. Chem.* **86**, 7681-7687 (2014).
28. Jia, H. P. & Quadrelli, E. A. Mechanistic aspects of dinitrogen cleavage and hydrogenation to produce ammonia in catalysis and organometallic chemistry: relevance of metal hydride bonds and dihydrogen. *Chem. Soc. Rev.* **43**, 547-564 (2014).
29. Ballmann, J., Munhá, R. F. & Fryzuk, M. D. The hydride route to the preparation of dinitrogen complexes. *Chem. Commun.* **46**, 1013-1025 (2010).
30. Shima, T. *et al.* Dinitrogen cleavage and hydrogenation by a trinuclear titanium polyhydride complex. *Science* **340**, 1549-1552 (2013).
31. Shima, T., Luo, G., Hu, S., Luo, Y. & Hou, Z. Experimental and computational studies of dinitrogen activation and hydrogenation at a tetranuclear titanium imide/hydride framework. *J. Am. Chem. Soc.* **141**, 2713-2720 (2019).
32. Deegan, M. M. & Peters, J. C. Electrophile-promoted Fe-to-N_2 hydride migration in highly reduced Fe(N_2)(H) complexes. *Chem. Sci.* **9**, 6264-6270 (2018).
33. Knoth, W. H. Dihydrido (dinitrogen) tris (triphenylphosphine) ruthenium. Dinitrogen bridging ruthenium and boron. *J. Am. Chem. Soc.* **94**, 104-109 (1972).
34. Rod, T. H., Logadottir, A. & Nørskov, J. K. Ammonia synthesis at low temperatures. *J. Phys. Chem.* **112**, 5343-5347 (2000).
35. Garden, A. L. & Skúlason, E. The mechanism of industrial ammonia synthesis revisited: calculations of the role of the associative mechanism. *J. Phys. Chem. C* **119**, 26554-26559 (2015).
36. Castleman Jr, A. & Keesee, R. Clusters: bridging the gas and condensed phases. *Acc. Chem. Res.* **19**, 413-419 (1986).

37. Rodriguez, M. M., Bill, E., Brennessel, W. W. & Holland, P. L. N_2 reduction and hydrogenation to ammonia by a molecular iron-potassium complex. *Science* **334**, 780-783 (2011).
38. Falcone, M., Chatelain, L., Scopelliti, R., Živković, I. & Mazzanti, M. Nitrogen reduction and functionalization by a multimetallic uranium nitride complex. *Nature* **547**, 332 (2017).
39. McEnaney, J. M. *et al.* Ammonia synthesis from N_2 and H_2O using a lithium cycling electrification strategy at atmospheric pressure. *Energy Environm. Sci.* **10**, 1621-1630 (2017).
40. Sato, T. *et al.* Raman and Infrared spectroscopic studies on Li_4RuH_6 combined with first-principles calculations. *Mater. Trans.* ***55***, 1117-1121 (2014).
41. Kritikos, M. & Nore´us, D. Synthesis and characterization of ternary alkaline-earth transition-metal hydrides containing octahedral $[Ru(II)H_6]^{4-}$ and $[Os(II)H_6]^{4-}$ complexes. *J. Solid State Chem.* **93**, 256-262 (1991).
42. Gao, W. *et al.* Barium hydride-mediated nitrogen transfer and hydrogenation for ammonia synthesis: a case study of cobalt. *ACS Catal.* **7**, 3654-3661 (2017).
43. Guan, H. *et al.* Preparation of nanometer magnesia with high surface area and study on the influencing factors of the preparation process. *Acta Phys-Chim Sin.* **22**, 804-807 (2006).
44. Ju, X. *et al.* Mesoporous Ru/MgO prepared by a deposition-precipitation method as highly active catalyst for producing CO_x-free hydrogen from ammonia decomposition. *Appl. Catal. B-Environ.* **211**, 167-175 (2017).
45. Toebes, M. L., Prinsloo, F. F., Bitter, J. H., van Dillen, A. J. & de Jong, K. P. Influence of oxygen-containing surface groups on the activity and selectivity of carbon nanofiber-supported ruthenium catalysts in the hydrogenation of cinnamaldehyde. *J. Catal.* **214**, 78-87 (2003).
46. Gao, W. *et al.* Production of ammonia via a chemical looping process based on metal imides as nitrogen carriers. *Nat. Energy* **3**, 1067-1075 (2018).
47. Bösenberg, U. *et al.* Characterization of metal hydrides by in-situ XRD. *Int. J. Hydrogen Energy* **39**, 9899-9903 (2014).
48. Hua, L. *et al.* Single photon ionization and chemical ionization combined ion source based on a vacuum ultraviolet lamp for orthogonal acceleration time-of-flight mass spectrometry. *Anal. Chem.* **83**, 5309-5316 (2011).
49. Qin, Z., Wu, X. & Tang, Z. Note: A novel dual-channel time-of-flight mass spectrometer for photoelectron imaging spectroscopy. *Rev. Sci. Instrum.* **84**, 066108 (2013).
50. Rapp, W. *et al.* α- and neutron-induced reactions on ruthenium isotopes. *Phys. Rev. C* **66**, 015803 (2002).
51. Andersen, S. Z. *et al.* A rigorous electrochemical ammonia synthesis protocol with quantitative isotope measurements. *Nature* **570**, 504-508 (2019).
52. Anderson, J. S., Rittle, J. & Peters, J. C. Catalytic conversion of nitrogen to ammonia by an iron model complex. *Nature* **501**, 84-87 (2013).
53. Liu, J. *et al.* Nitrogenase-mimic iron-containing chalcogels for photochemical reduction of dinitrogen to ammonia. *Proc. Natl. Acad. Sci. U.S.A.* **113**, 5530-5535 (2016).
54. Blöchl, P. E. Projector augmented-wave method. *Phys. Rev. B* **50**, 17953-17979 (1994).
55. Kresse, G. & Joubert, D. From ultrasoft pseudopotentials to the projector augmented-wave method. *Phys. Rev. B* **59**, 1758-1775 (1999).
56. Kresse, G. & Furthmüller, J. Efficient iterative schemes for ab initio total-energy calculations using a plane-wave basis set. *Phys. Rev. B* **54**, 11169-11186 (1996).
57. Cramer, C. J. Ed., *Essentials of computational chemistry* 2nd edn (Wiley, 2004).
58. Sprowl, L. H., Campbell, C. T. & Árnadóttir, L. Hindered translator and hindered rotor models for adsorbates: partition functions and entropies. *J. Phys. Chem. C* **120**, 9719-9731 (2016).
59. Sprowl, L. H., Campbell, C. T. & Arnadottir, L. Correction to "hindered translator and hindered rotor models for adsorbates: partition functions and entropies". *J. Phys. Chem. C* **121**, 9655-9655 (2017).
60. Campbell, C. T., Sprowl, L. H. & Árnadóttir, L. Equilibrium constants and rate constants for adsorbates: two-dimensional (2D) ideal gas, 2D ideal lattice gas, and ideal hindered translator models. *J. Phys. Chem. C* **120**, 10283-10297 (2016).
61. Henkelman, G., Uberuaga, B. P. & Jónsson, H. A climbing image nudged elastic band method for finding saddle points and minimum energy paths. *J. Chem. Phys.* **113**, 9901-9904 (2000).

Acknowledgments

The authors acknowledge the beam time of Shanghai Synchrotron Radiation Facility and Deutsches Elektronen-Synchrtron and the help of Jo-Chi Tseng and Jozef Bednarcik for *in situ* SR-PXD. P.C. and J.G. thank the financial support from National Natural Science Foundation of China (Grant Nos. 21988101, 21633011 and 21922205), Dalian Institute of Chemical Physics (DCLS201701), K. C. Wong Education Foundation (GJTD-2018-06) and 2011-iChEM; J.P, H.H and T.V. thank the Velux Foundations for financial support through the research center V-Sustain (#9455).

Author contributions

P.C. conceived the idea. P.C. and T.V. supervised the research and wrote the paper. Q.W. conducted most of the experimental work and prepared SI. J.P. conducted DFT calculations and co-prepared SI. J.G. supervised the experimental work. H.H. supervised the theory work. H.X. and L.J. for GOS-MS. L.H. and H.L. for CTI-TOFMS. All authors participated the discussion and data analyses.

Competing interests

Authors declare no competing interests.

Supplementary information

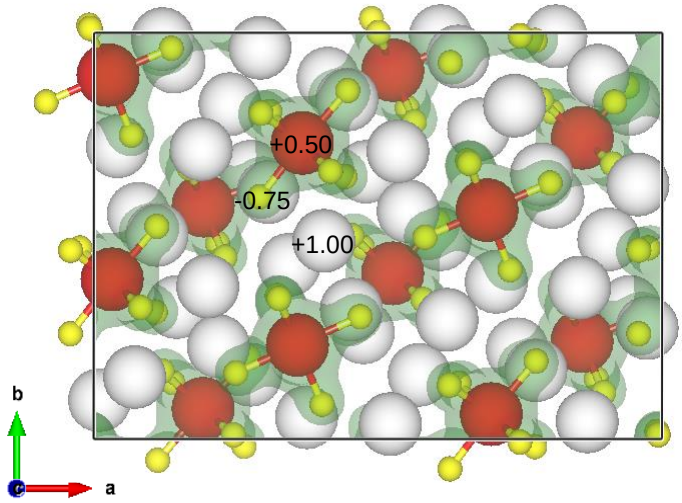

Supplementary Fig. 1. Electronic properties of stoichiometric Li_4RuH_6 surface. The charge density plot of Li_4RuH_6 surface with Bader charge analyses on Ru (red), Li (white) and H (yellow).

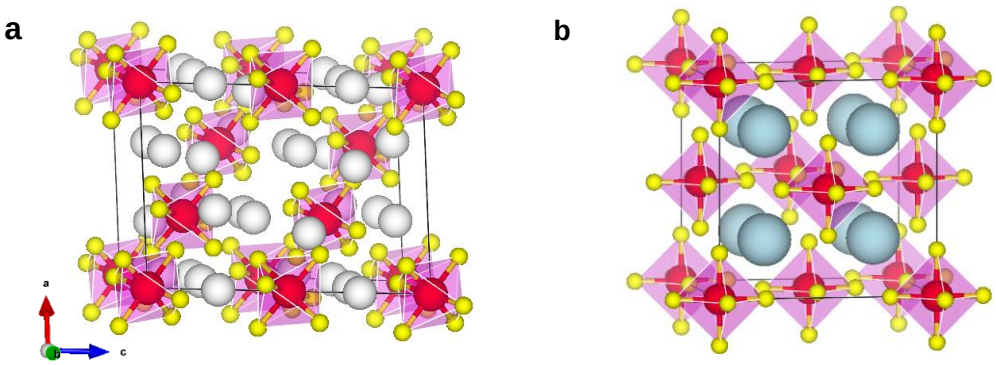

(a) Li_4RuH_6		Lattice parameters						Bond distance (Å)	
		a(Å)	b(Å)	c(Å)	α(°)	β(°)	γ(°)	d_{Ru-H}	d_{Ru-Li}
Theory (This work)		8.279	8.279	10.169	90	90	120	1.725	2.542
Experiment[1-2]		8.169	8.169	10.025	90	90	120	1.74	
(b) Ba_2RuH_6		Lattice parameters						Bond distance (Å)	
		a(Å)	b(Å)	c(Å)	α(°)	β(°)	γ(°)	d_{Ru-H}	d_{Ru-Ba}
Theory	This work	8.083	8.083	8.083	90	90	90	1.74	3.51
	Refs.	8.052[3], 8.092[4]	8.052[3], 8.092[4]	8.052[3], 8.092[4]	90[3-4]	90[3-4]	90[3-4]	1.74[3]	3.49[3]
Experiment[5]		8.028	8.028	8.028	90	90	90		

Supplementary Fig. 2. The crystal structures and related parameters of Li_4RuH_6 (a) and Ba_2RuH_6 (b). The Ru, Li, Ba and H atoms are presented by red, white, steel grey and yellow balls.

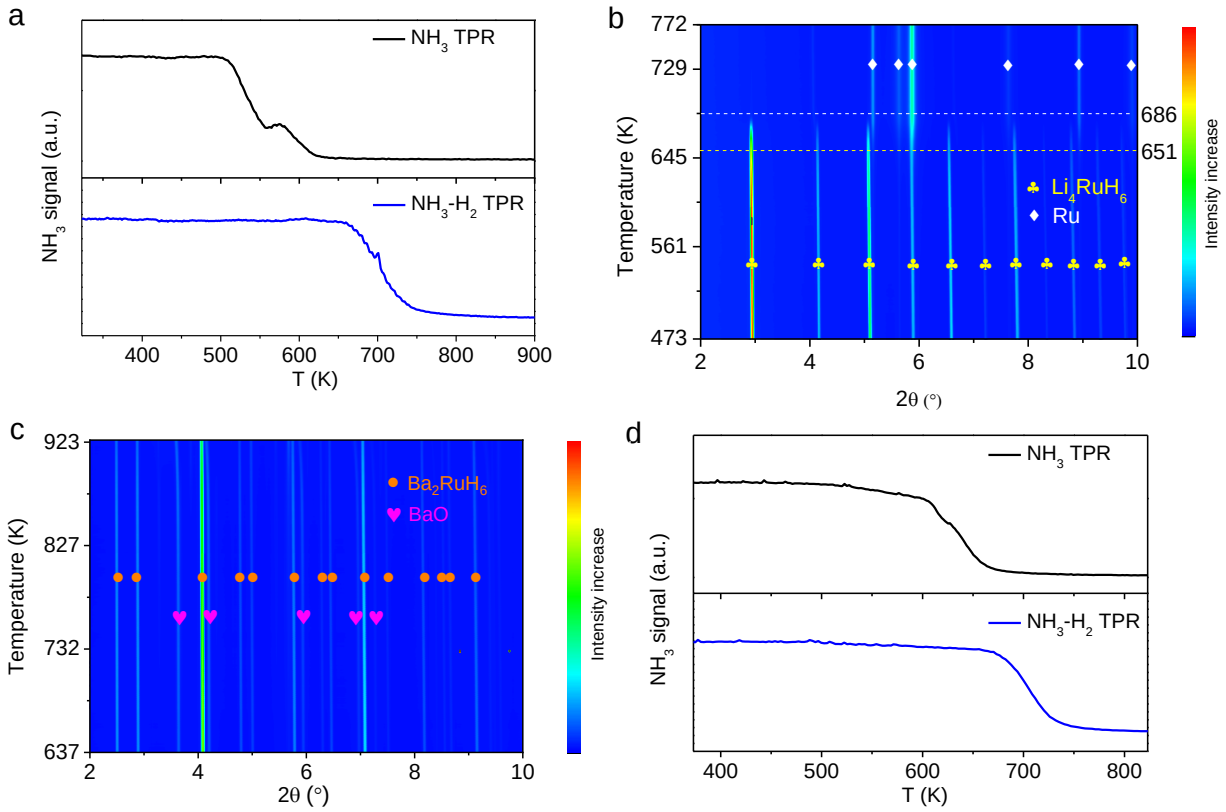

Supplementary Fig. 3. The stability of bulk Li_4RuH_6 and Ba_2RuH_6 under different conditions. a, TPR profile of Li_4RuH_6 in a mixture gas of NH_3-Ar (NH_3:Ar=0.5:99.5) and a mixture gas of NH_3-H_2-Ar (NH_3:H_2:Ar=0.5:75:24.5). **b**, *In situ* SR-PXD characterization of Li_4RuH_6 sample under atmospheric N_2 and elevated temperatures (from 473 K to 773 K). **c**, *In situ* SR-PXD characterization of Ba_2RuH_6 sample under atmospheric N_2-3H_2 mixture and elevated temperatures (from 637 K to 923 K). **d**, TPR profile of Ba_2RuH_6 in a mixture gas of NH_3-Ar (NH_3:Ar=0.5:99.5) and a mixture gas of NH_3-H_2-Ar (NH_3:H_2:Ar=0.5:75:24.5).

The above results show that the Li_4RuH_6 phase is stable up to ca. 651 K under N_2 atmosphere. While upon co-feeding H_2, it survives until 738 K (Fig. 1e). Li_4RuH_6 is also resistant to diluted NH_3 at temperature up to 500 K. While upon co-feeding with H_2, the temperature pulls ahead to 673 K. Ba_2RuH_6 phase is stable up to 923 K under atmospheric N_2-3H_2 mixture. Ba_2RuH_6 is also resistant to diluted NH_3 at temperatures up to 550 K. While upon co-feeding with H_2, the temperature pulls ahead to 673 K.

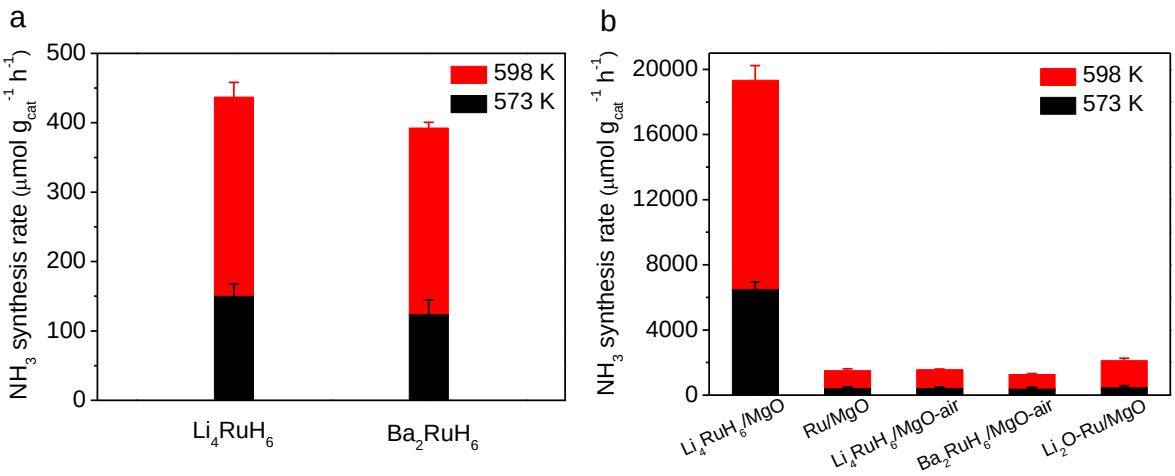

Supplementary Fig. 4. NH_3 synthesis rates at 573 and 598 K. a, bulk Li_4RuH_6 and Ba_2RuH_6 catalysts. **b**, Li_4RuH_6/MgO, Ru/MgO, Li_4RuH_6/MgO-air, Ba_2RuH_6/MgO-air and Li_2O-Ru/MgO catalysts (Reaction conditions: catalyst loading 30 mg, H_2:N_2=3:1, flow rate 30 ml min^{-1}, and 1 bar).

After exposed to air, the hydrides were oxidized and deactivated. The activities of Li_4RuH_6/MgO-air and Ba_2RuH_6/MgO-air samples are thus much lower and are similar to that of Ru/MgO.

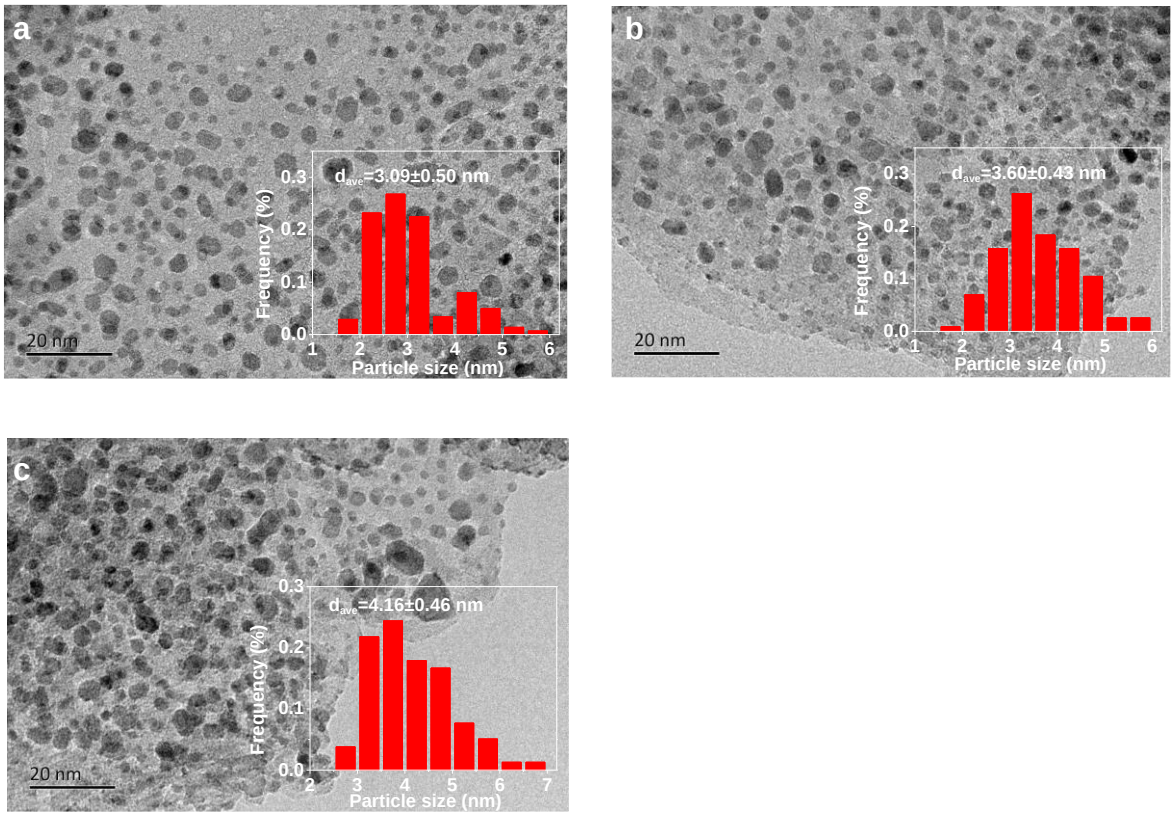

Supplementary Fig. 5. TEM observations. a, Ru/MgO. **b**, Li_4RuH_6/MgO. **c**, Ba_2RuH_6/MgO. The inset picture of each image shows the corresponding particle size distribution. The number of particles for each image surveyed was more than 100.

From the results of particle size distribution analyses, we can see that, after introducing Li and Ba to the parent Ru/MgO catalyst, there is a certain increase in the size of dark particles.

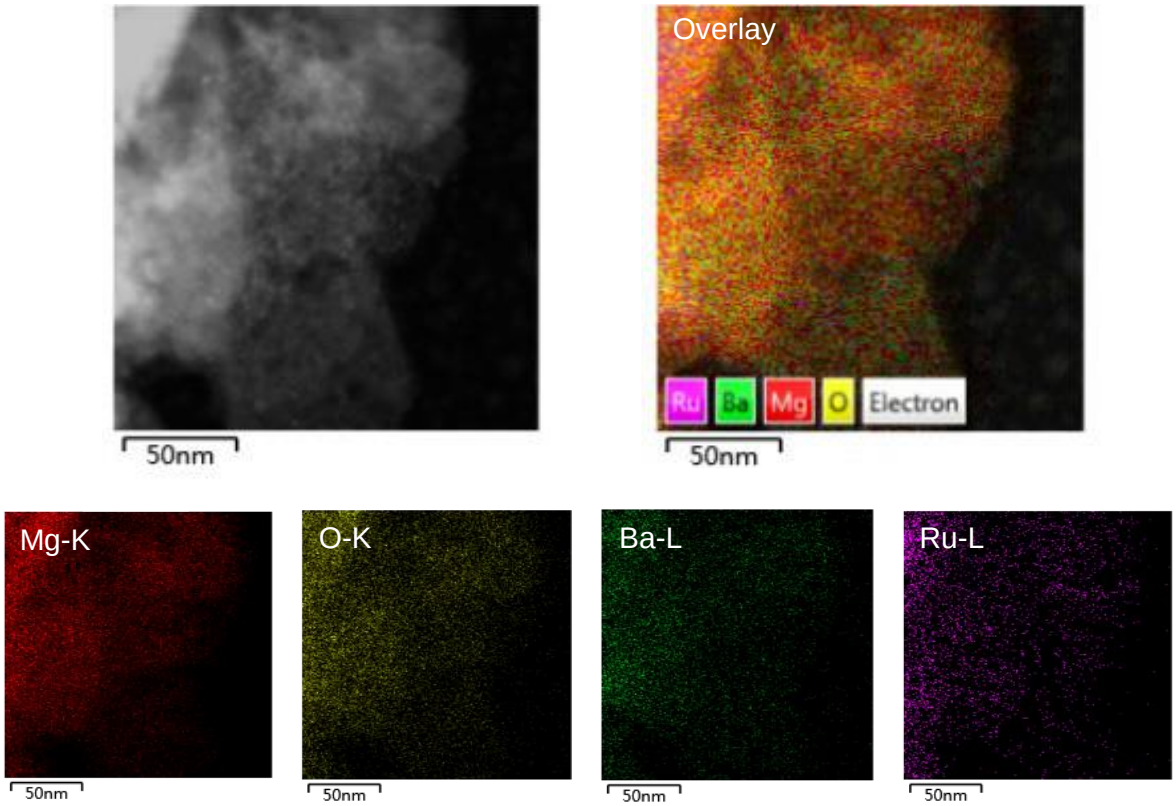

Supplementary Fig. 6. HAADF-STEM characterizations of the Ba_2RuH_6/MgO sample. STEM-EDS maps of Mg-K, O-K, Ba-L and Ru-L, and overlayed Mg, O, Ba and Ru are shown.

From the mapping results, we can see that Ba and Ru are in proximity and dispersed evenly over the MgO support. Li_4RuH_6/MgO sample was not characterized because Li is out of the analysis scope of EDS.

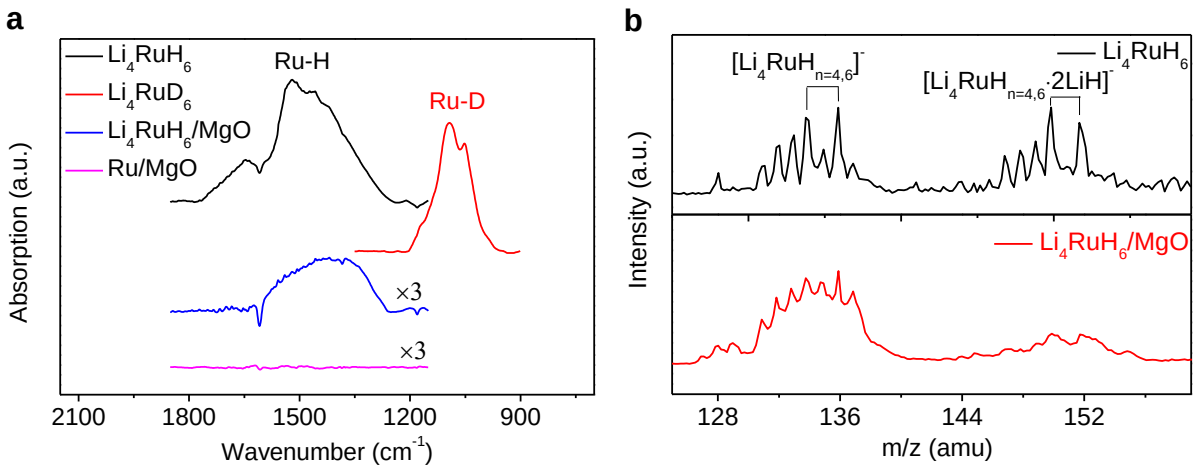

Supplementary Fig. 7. Characterization of the bulk and supported ternary hydride catalysts. a, DRIFT spectra of the as-prepared $Li_4RuH(D)_6$, Li_4RuH_6/MgO and Ru/MgO catalysts. **b**, Mass spectra of the species produced by pulsed laser vaporization of the Li_4RuH_6 and Li_4RuH_6/MgO targets in the presence of a He carrier gas.

Li_4RuH_6 surface has Ru-H stretching vibration in the range of 1200 to 1800 cm^{-1}, which is confirmed by Ru-D stretch in the deuterated sample. The Li_4RuH_6/MgO sample has a similar Ru-H stretching range as the bulk sample but somehow with red shift, which might be due to the elongated Ru-H bond after the particle size reduction to nanoscale. While for the reference sample Ru/MgO, there was no infrared absorption peak in the range of 1800-1200 cm^{-1}. The mass spectrum of Li_4RuH_6/MgO is similar to that of bulk phase Li_4RuH_6. These characterizations show that the supported catalyst resembles essentially to the bulk-phase Li_4RuH_6.

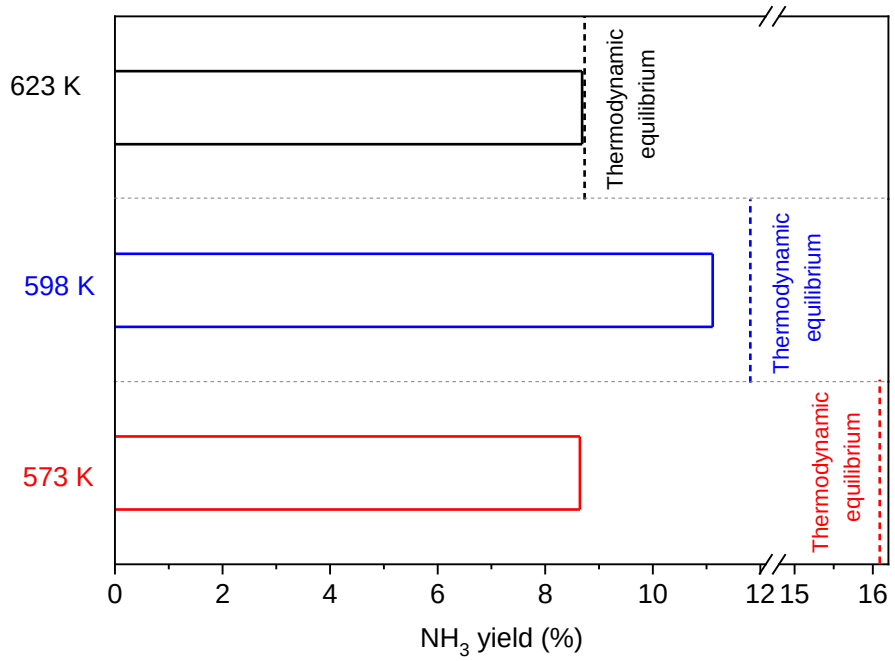

Supplementary Fig. 8. Temperature dependence of NH_3 yield of Ba_2RuH_6/MgO catalyst at 1 MPa. (Reaction conditions: H_2:N_2=2:3, WHSV=7500 ml g_{cat}^{-1} h^{-1})

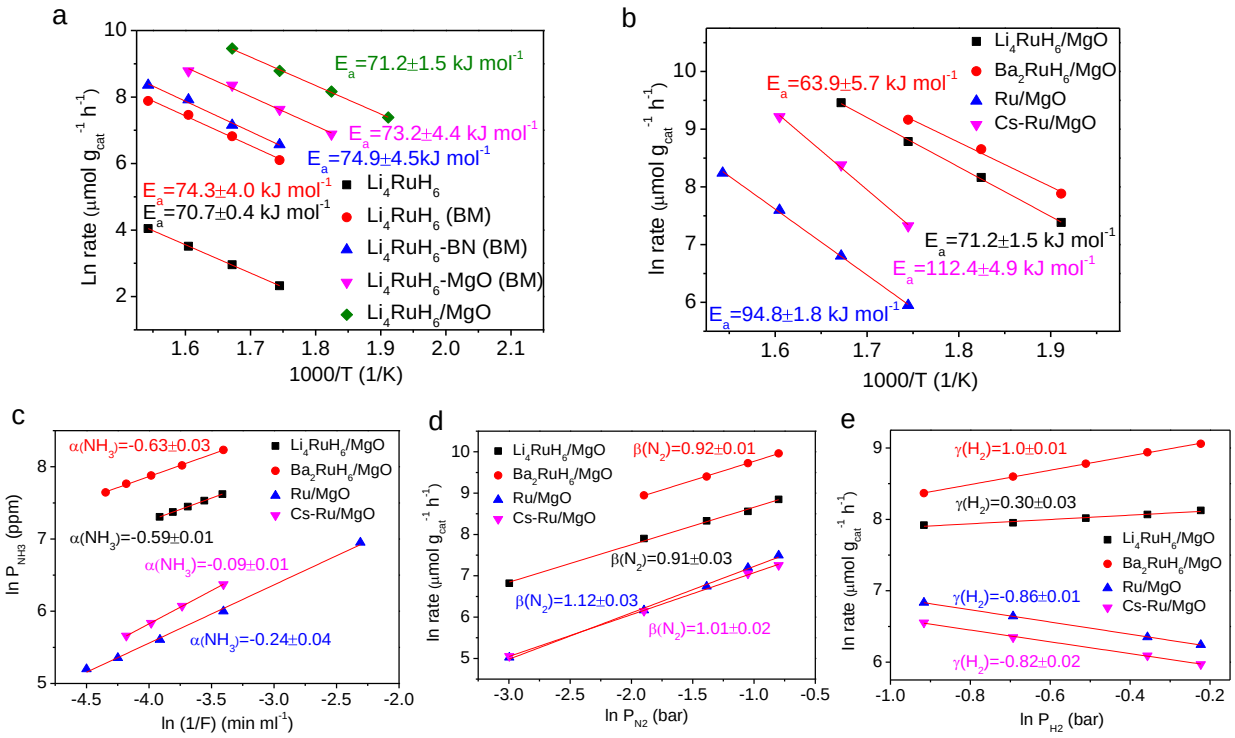

Supplementary Fig. 9. Measurements of kinetic parameters. a and **b** Arrhenius plots of the Li_4RuH_6, ball-milled Li_4RuH_6 (Li_4RuH_6 (BM)), ball-milled mixture of Li_4RuH_6 and BN (Li_4RuH_6-BN-(BM)), ball-milled mixture of Li_4RuH_6 and MgO (Li_4RuH_6-MgO-(BM)), Li_4RuH_6/MgO, Ba_2RuH_6/MgO, Ru/MgO and Cs-Ru/MgO catalysts. **c** to **e** Dependence of ammonia synthesis rates on the partial pressures of NH_3, N_2 and H_2, respectively, under a total pressure of 1 bar at 573 K over Li_4RuH_6/MgO, Ba_2RuH_6/MgO, Ru/MgO and Cs-Ru/MgO catalysts.

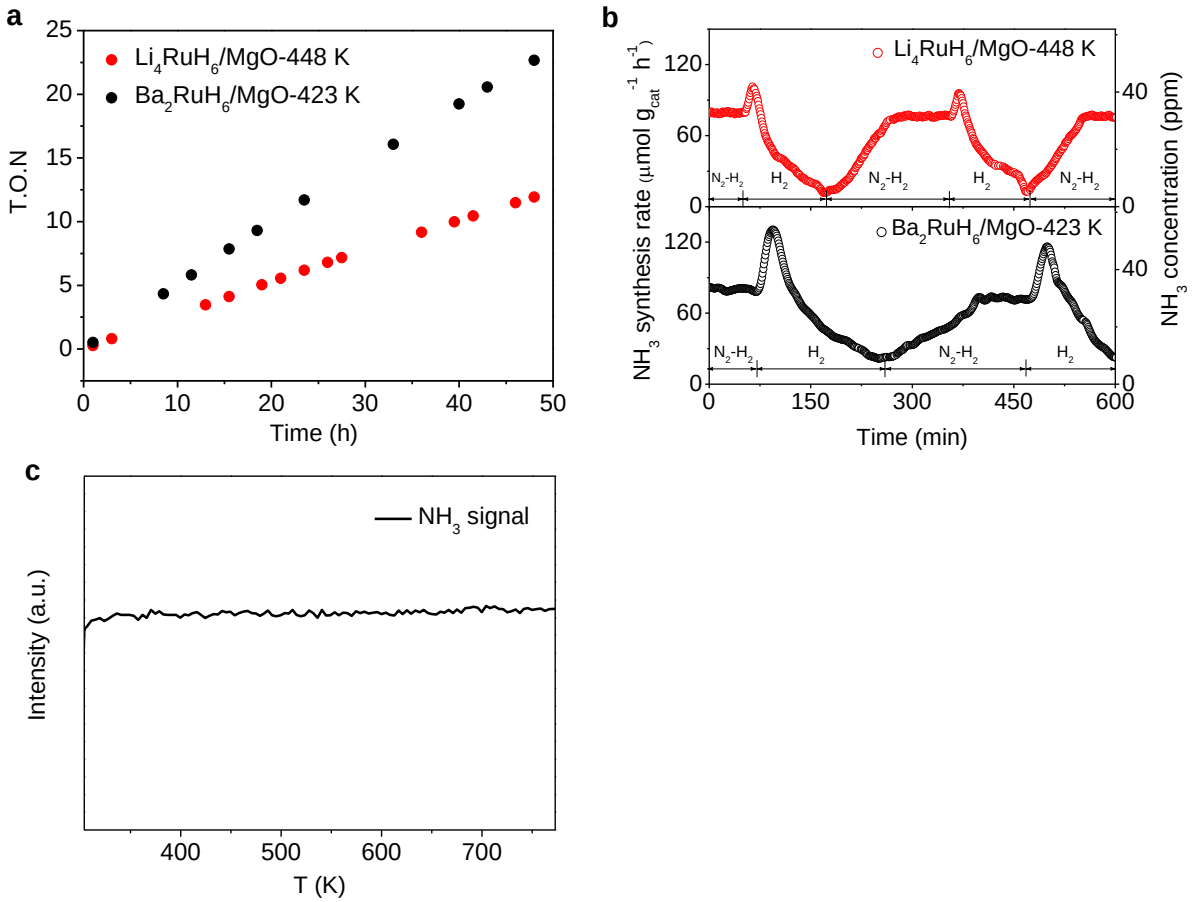

Supplementary Fig. 10. Low-temperature catalytic activity and stability. a, Time dependence of NH_3 synthesis TON (based on the amount of surface Ru estimated from the particle size observed by TEM) over Li_4RuH_6/MgO and Ba_2RuH_6/MgO catalysts at 448 K and 423 K, respectively (Reaction conditions: catalyst loading 30 mg, H_2:N_2=2:3, flow rate 30 ml min^{-1}, and 1 bar). These data evidence the catalytic formation of NH_3. **b**, Time course of ammonia synthesis rate of Li_4RuH_6/MgO at 448 K and Ba_2RuH_6/MgO at 423 K under an alternative feeding of N_2-H_2 (H_2:N_2=2:3) and pure H_2 streams (Reaction conditions: catalyst loading 30 mg, flow rate 30 ml min^{-1}, and 1 bar). Upon switching from N_2-H_2 steam to pure H_2 steam, there is a rapid increase in the NH_3 production rate because the sudden increase of H_2 content (from 40% to 100%) speeds up the release rate of NH_3. **c**, MS spectrum of the temperature-programmed reaction of N_2 with Li_4RuH_6/MgO. No ammonia was detectable showing lattice H cannot work alone for ammonia formation.

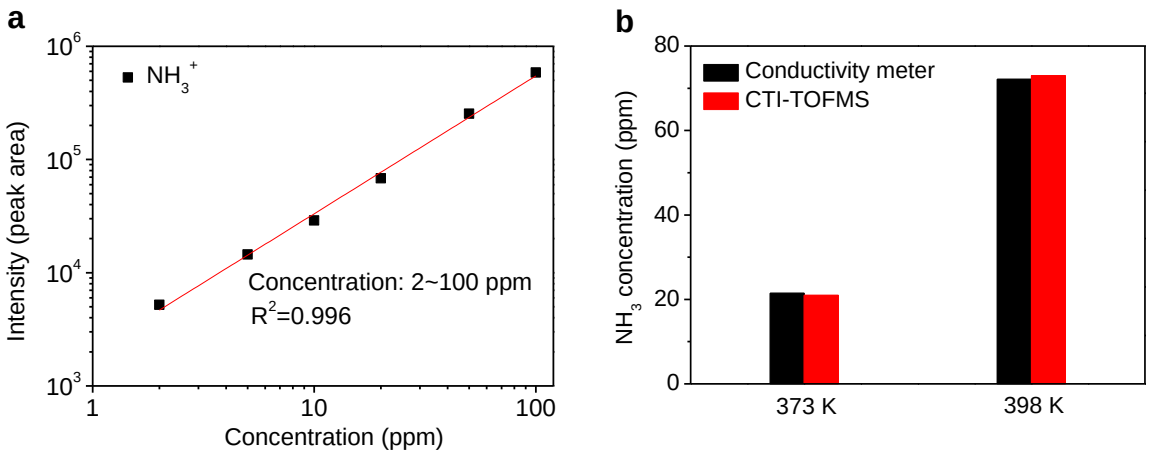

Supplementary Fig. 11. Low-temperature catalytic performance characterized by CTI-TOFMS. a, Linear calibration curve for NH_3^+ in the concentration range of 2 to 100 ppm of the CTI-TOFMS. **b**, Activities of Ba_2RuH_6/MgO catalyst measured by conductivity meter and CTI-TOFMS at 373 and 398 K, respectively (Reaction conditions: catalyst loading 200 mg, H_2:N_2=1:3, flow rate 36 ml min^{-1}, and 1 bar).

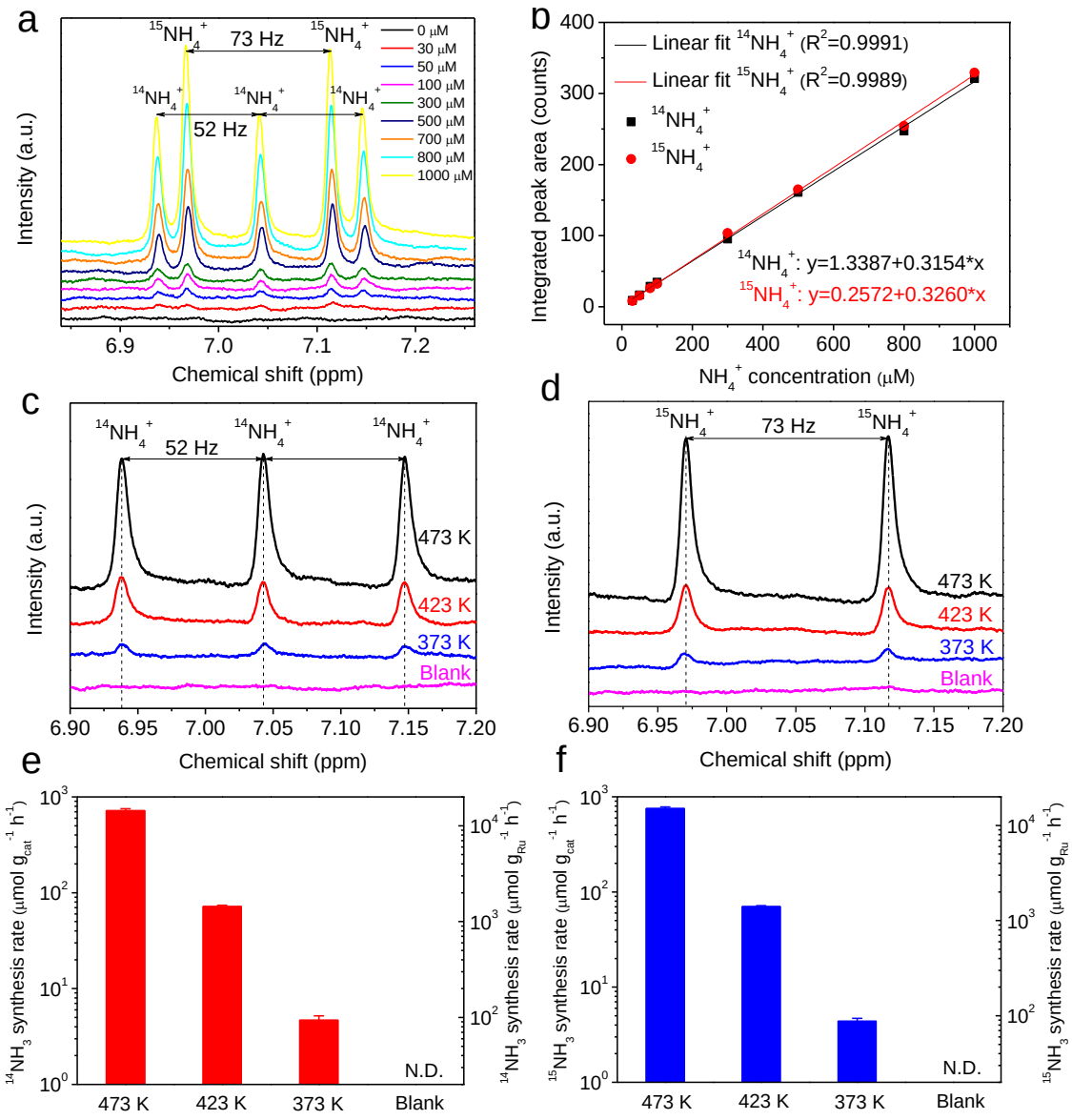

Supplementary Fig. 12. Quantification of low-temperature NH_3 synthesis rates using ^{1}H-NMR spectroscopy. a, ^{1}H NMR spectra of a series of $^{14}NH_4Cl$ and $^{15}NH_4Cl$ solutions (with equimolar concentrations of $^{14}NH_4^+$ and $^{15}NH_4^+$) with different concentrations. **b**, Linear calibration curves for both $^{14}NH_4^+$ and $^{15}NH_4^+$ in the concentration range of 30 to 1000 μM. After absorbing outlet gas at 373K, 423 K and 473 K, respectively, the sulfuric acid solutions were collected for ^{1}H-NMR measurements, showing in **c** and **d** are the ^{1}H-NMR spectra of $^{14}NH_4^+$ and $^{15}NH_4^+$ signals, **e** and **f** are the corresponding $^{14}NH_3$ and $^{15}NH_3$ synthesis rates derived from ^{1}H-NMR. Conditions: Ba_2RuH_6/MgO catalyst 30mg, H_2 : $^{14}N_2$($^{15}N_2$) = 2 : 3, flow rate 10 ml min^{-1}, 1 bar. 4 mL diluted sulfuric acid solution was used to absorb the produced NH_3. The absorption time is 10 min at 473 K, 30 min at 423 K and 120 min at 373 K, respectively. Blank experiment (without catalyst loading) was performed at 298 K for 120 min, where NH_3 concentration is below the detection limit.

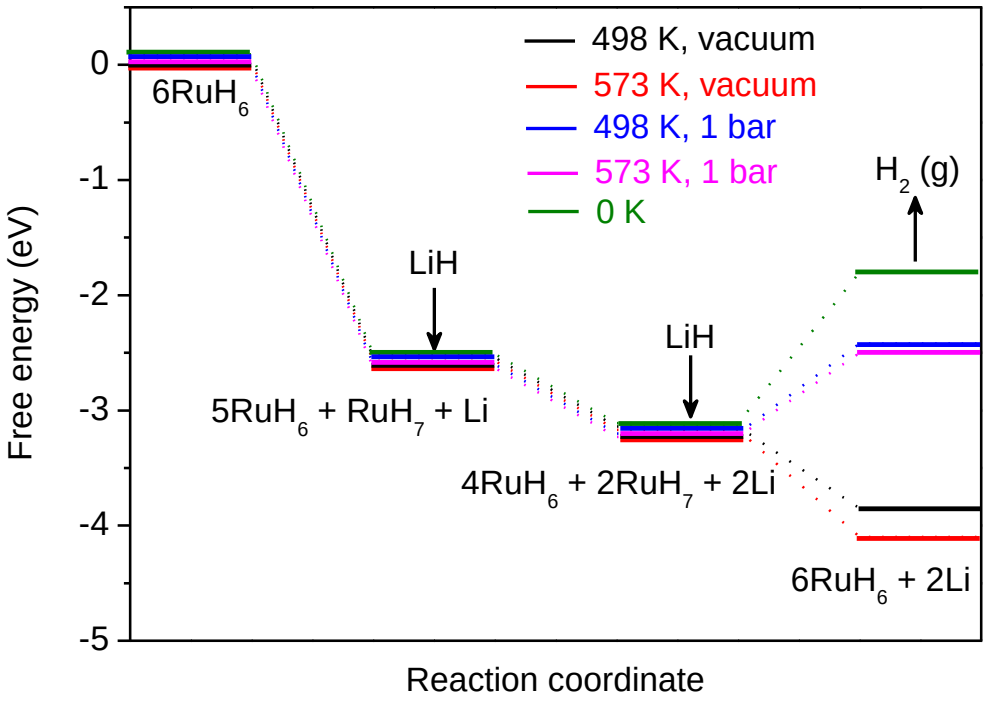

Supplementary Fig. 13. The free energy plots of LiH adsorption on the stoichiometric Li_4RuH_6 surface under different conditions. LiH dissociates exothermically into surface Li and the H goes to one of the neighboring RuH_6 sites creating a [RuH_7]. Adding two extra LiH to the surface results in the composition of $4RuH_6 + 2RuH_7 + 2LiH$ that is thermodynamically stable under the reaction condition applied in this study (373 K to 573 K, ≥ 1 bar). However, further adding LiH will block the surface from N_2 adsorption.

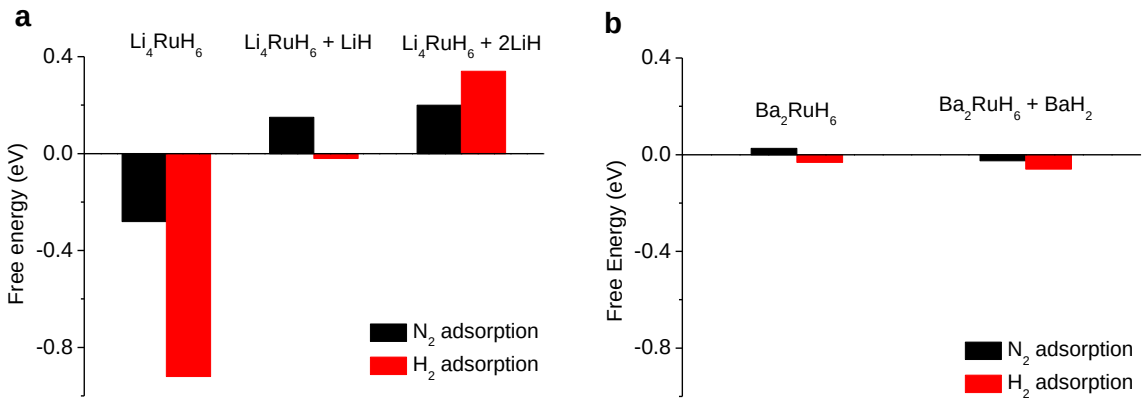

Supplementary Fig. 14. Competitive H_2(g) and N_2(g) adsorption on ternary hydride surface. **a**, Li_4RuH_6 surface with and without extra LiH. **b**, Ba_2RuH_6 surface with and without extra BaH_2. Our free energy calculations show that H_2 adsorption is strongly favored over N_2 adsorption on the stoichiometric Li_4RuH_6 surface; while on the over-stoichiometric surface especially on the Li_4RuH_6 surface with two extra LiH, N_2 adsorption is preferred to H_2 adsorption. The competitive adsorption of N_2 and H_2 is not pronounced over the stoichiometric Ba_2RuH_6, however, the addition of excess BaH_2 enhances N_2 adsorption, which may account for its higher TOF.

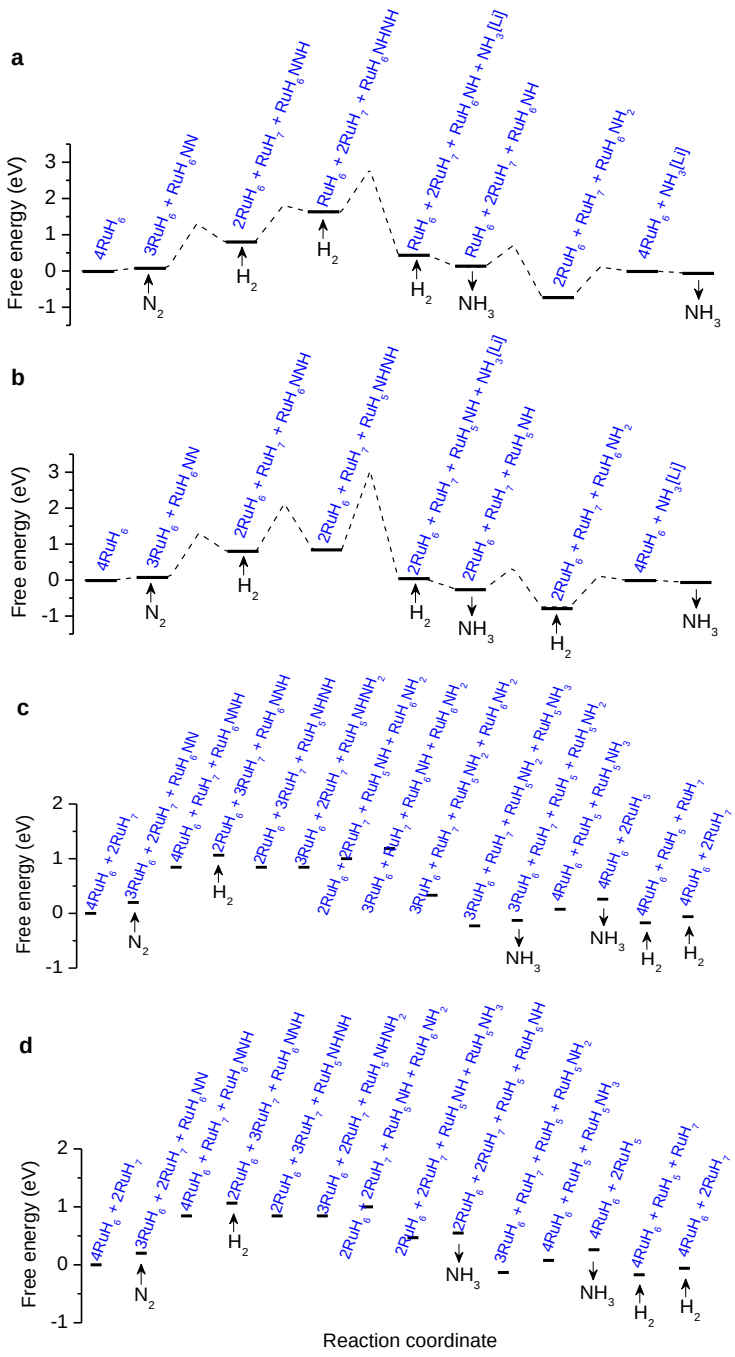

Supplementary Fig. 15. A few possible pathways for N_2 activation and hydrogenation on Li_4RuH_6 surface. The free energy profiles of **a** and **b** are based on a model of Li_4RuH_6 (110) surface composed of four Li_4RuH_6 units and stabilized by one extra LiH. The calculated energy span for these two paths are 3.50 eV and 3.72 eV, respectively. The free energy profiles of **c** and **d** (without kinetic barriers) are based on a model of (110) surface with six Li_4RuH_6 units and stabilized by two extra LiH. All free energy pathways are calculated at 573 K and 1 bar (H_2:N_2 ratio is fixed at 3, and the concentration of NH_3 is 0.27% that is consistent with the experimental condition.)

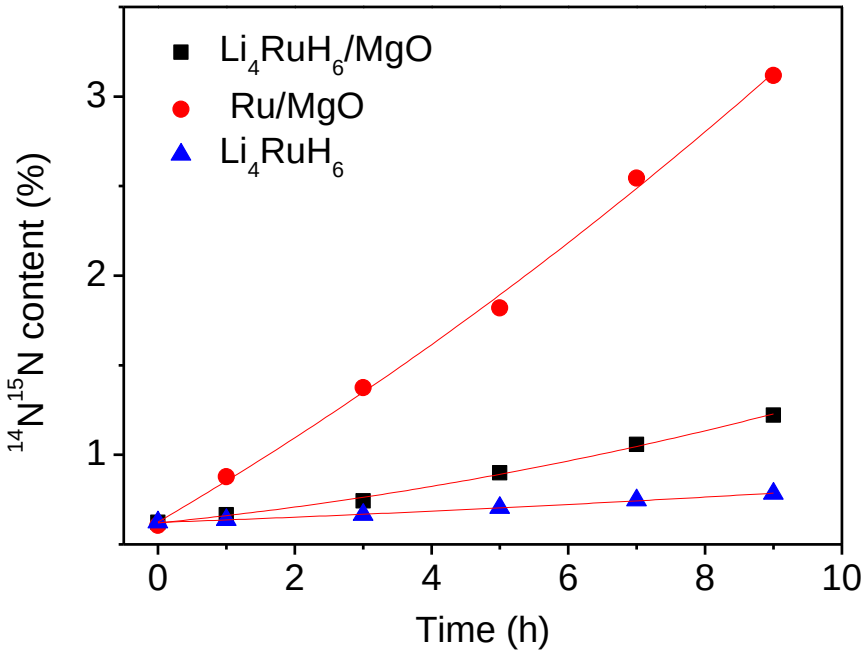

Sample	Fitting curve	Correlation coefficient (R^2)	Initial N_2 exchange rate at 473 K ($\mu mol\ g_{cat}^{-1}\ h^{-1}$)
Li_4RuH_6/MgO	$y = 0.620 + 0.0377x + 3.33*10^{-3}x^2$	0.996	1.4
Ru/MgO	$y = 0.625 + 0.223x + 6.22*10^{-3}x^2$	0.996	5.2
Li_4RuH_6	$y = 0.622 + 0.0139x + 4.76*10^{-4}x^2$	0.997	0.065

Supplementary Fig. 16. N_2 exchange reactions. Time course of $^{14}N^{15}N$ formation over Li_4RuH_6/MgO, Ru/MgO and Li_4RuH_6 catalysts at 473 K. The data were fitted by high-order polynomial curves for easy analysis and the fitting results were shown in the table below the figure. The initial N_2 exchange rates for Li_4RuH_6/MgO, Ru/MgO and Li_4RuH_6 at 473 K can be estimated by derivation the fitting curves at the initial time.

It should be noted that the possible inhomogeneity of the Li_4RuH_6/MgO sample and its partial decomposition to LiH and Ru at 473K may contribute to the formation of $^{14}N^{15}N$.

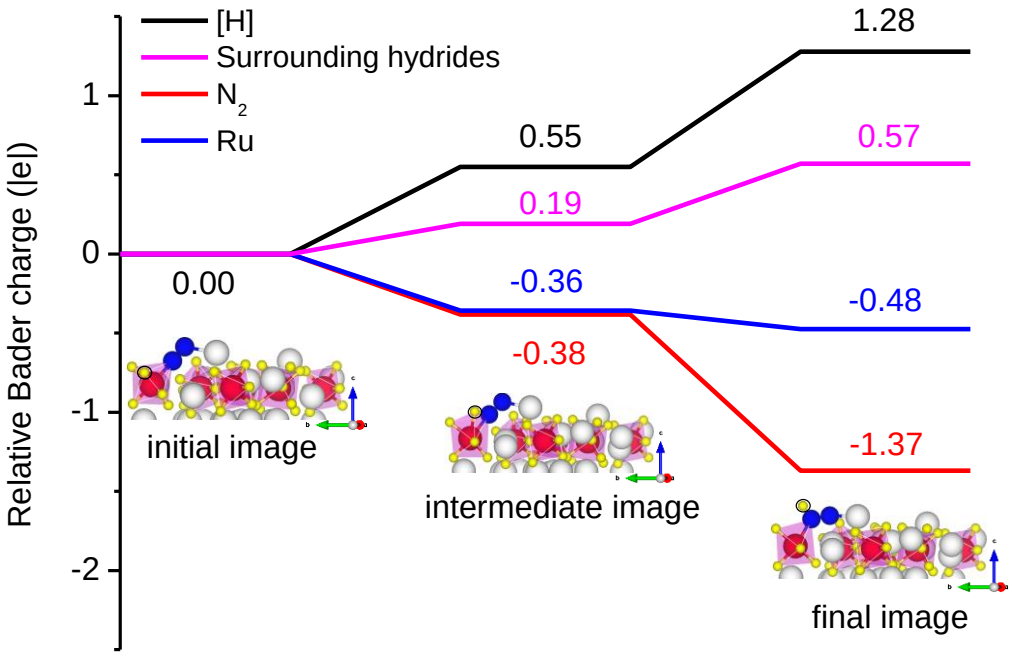

Supplementary Fig. 17. Bader charge analyses of the first hydrogenation step (1-2). In this process, the adsorbed N_2 gains substantial electron from the transiting lattice hydride (denoted as [H]). It should be noted that the changes in Bader charge (i.e., relative Bader charge) along the path is relative to the initial image. The particular lattice hydride of interest is marked by a black round ring.

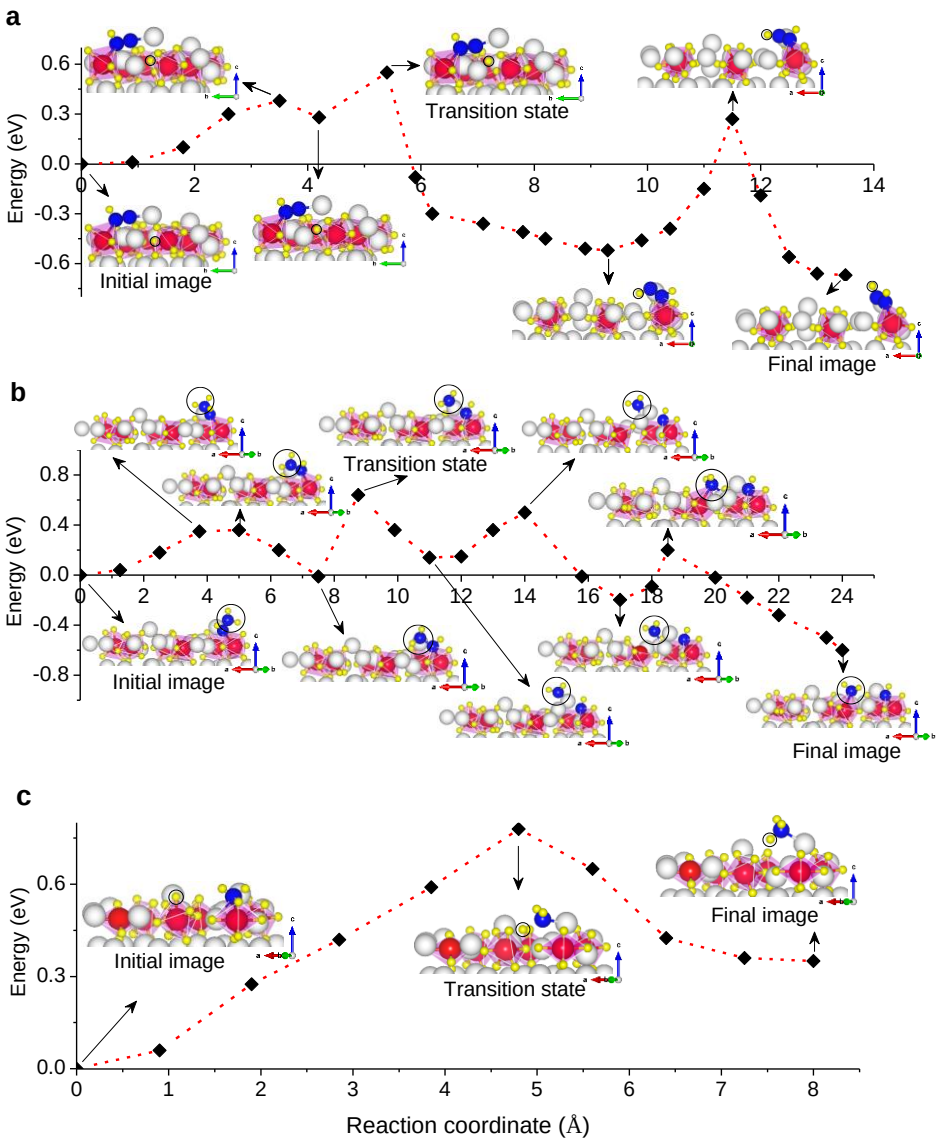

Supplementary Fig. 18. Detailed kinetic paths of some characteristic steps of the catalysis over Li_4RuH_6 surface. a, Kinetic path of the lattice transfer of step **2-3**. Li cations mediate lattice H transfer from [RuH_7] complex to -NHN species that is bonded on [RuH_5] site and thus forming -NHNH species. **b**, Kinetic path of the N-N dissociation step **5-6**. The N-N bond dissociates via a Li-assisted multi-step path, creating a [RuH_5]-NH and a [RuH_6]-NH_2 species. **c**, Kinetic path of the second NH_3 formation step **9-10**. Li cations mediate lattice H transfer from [RuH_7] complex to -NH_2 species and thus forming the second NH_3, during which NH_3 leaves the [RuH_5] site and hangs loosely on the neighboring Li. The particular H atom or NH_2 species of interest is marked by a black round ring.

Supplementary Table 1. Thermodynamic calculations of the reactions for the formation of Li_4RuH_6 and Ba_2RuH_6. The reaction enthalpy of formation of Li_4RuH_6 ($\Delta_rH^0(Li_4RuH_6)$) is obtained by the corresponding van't Hoff plots in Fig.1d. The reaction enthalpy of formation of Ba_2RuH_6 ($\Delta_rH^0(Ba_2RuH_6)$) is taken from Ref.[6]. The standard enthalpies of formation of other substances are taken from "NIST Standard Reference Number 69". Therefore, the standard enthalpies of formation of Li_4RuH_6 ($\Delta_fH^0(Li_4RuH_6)$) and Ba_2RuH_6 ($\Delta_fH^0(Ba_2RuH_6)$) can be evaluated by combining the Δ_rH^0 and Δ_fH^0 values.

Reaction	4LiH	+	Ru	+	H_2	→	Li_4RuH_6	Δ_rH^0 (kJ mol^{-1})
Δ_fH^0 (kJ mol^{-1})	-90.5		0		0		-455.1	-93.1
Reaction	$2BaH_2$	+	Ru	+	H_2	→	Ba_2RuH_6	Δ_rH^0 (kJ mol^{-1})
Δ_fH^0 (kJ mol^{-1})	-178.3		0		0		-464.1	-107.5

Supplementary Table 2. Physicochemical properties of the as-prepared Ru-based catalysts.

Catalyst	Ru content (wt %)	S_{BET}[a] ($m^2\ g^{-1}$)	d[b] (nm)	D[b] (%)	Surface Ru content[b] (wt %)
Li_4RuH_6/MgO	8.0	245.5	3.60	36.9	2.95
Ba_2RuH_6/MgO	5.0	154.1	4.16	32.0	1.60
Ru/MgO	8.7	266.6	3.09	43.0	3.74
Cs-Ru/MgO	7.3	43.0	6.02	22.1	1.61
Li_4RuH_6	---	7.2	---	---	---
Ba_2RuH_6	---	4.8	---	---	---

[a]BET specific surface area.
[b]Mean Ru particle size (d), dispersion (D) and surface Ru content were estimated based on TEM data assuming spherical metal particles.

Supplementary Table 3. Ammonia synthesis over recently developed Ru-based catalysts.

Catalysts	Metal content (wt %)	r_{NH3}[a] (mmol g_{Ru}^{-1} h^{-1})		WHSV (ml g^{-1} h^{-1})	Ref.
		573 K, 10 bar	573 K, 1 bar		
Li_4RuH_6/MgO	8.0	275	114	60000	this work
Ba_2RuH_6/MgO	5.0	680	276	60000	
Ru/$C_{12}A_7$:e^-	1.8	94 (593 K)	41	36000	7
Ru/Ca_2N:e^-	1.8	228 (593 K)	93	36000	7
Ru/$BaTiO_{2.5}H_{0.5}$	2.5	---	19 (598 K)	66000	8
Ru/$Ca(NH_2)_2$	10	158 (8 bar)	56	36000	9
Ru/Ba-$Ca(NH_2)_2$	10	233 (9 bar)	90	36000	10
Ru/Pr_2O_3	5	18 (9 bar)	---	18000	11
Ru/$La_{0.5}Ce_{0.5}O_{1.75}$	5	22	---	72000	12
Ru/BaO-CaH_2	10	165 (9 bar)	69	36000	13
Ru/$BaCeO_{3-x}N_yH_z$	4.5	111 (9 bar)	---	36000	14
Ba-Ru-Li/AC	4.8	---	1.5	62400	15
LaRuSi	37.7	---	4.7 (673 K)	36000	16

[a]Ammonia synthesis rates per gram of Ru under 573 K, 10 bar and 573 K, 1bar (H_2:N_2=3 or 2/3), unless otherwise stated.

Supplementary references

1. Kritikos, M., Nore´us, D., Andresen, A. F. & Fischer, P. Preparation and structure of the ternary hydrides Li_4RuH_6, Na_4RuH_6, and Li_4OsH_6 containing octahedral transition metal hydrogen complexes. *J. Solid State Chem.* 92, 514-519 (1991).
2. Sato, T. *et al.* Raman and Infrared spectroscopic studies on Li_4RuH_6 combined with first-principles calculations. *Mater. Trans. 55*, 1117-1121 (2014).
3. Orgaz, E. & Aburto, A. Electronic structure of ternary ruthenium-based hydrides. *J. Phys. Chem. C* 112, 15586-15594 (2008).
4. Kadir, K., Moser, D., Münzel, M. & Noréus, D. Investigation of counterion influence on an octahedral IrH_6-complex in the solid state hydrides $AAeIrH_6$ (A = Na, K and Ae = Ca, Sr, Ba, and Eu) with a new structure type. *Inorg. Chem.* 50, 11890-11895 (2011).
5. Kritikos, M. & Nore´us, D. Synthesis and characterization of ternary alkaline-earth transition-metal hydrides containing octahedral $[Ru(II)H_6]^{4-}$ and $[Os(II)H_6]^{4-}$ complexes. *J. Solid State Chem.* 93, 256-262 (1991).
6. Nicholson, K. M. & Sholl, D. S. First-principles screening of complex transition metal hydrides for high temperature applications. *Inorg. Chem.* 53, 11833-11848 (2014).
7. Kitano, M. *et al*. Essential role of hydride ion in ruthenium-based ammonia synthesis catalysts. *Chem. Sci.* 7, 4036-4043 (2016).
8. Tang, Y. *et al*. Metal-dependent support effects of oxyhydride-supported Ru, Fe, Co catalysts for ammonia synthesis. *Adv. Energy Mater.* 8, 1801772 (2018).
9. Inoue, Y. *et al.* Efficient and stable ammonia synthesis by self-organized flat Ru nanoparticles on calcium amide. *ACS Catal.* 6, 7577-7584 (2016).
10. Kitano, M. *et al*. Self-organized ruthenium–barium core–shell nanoparticles on a mesoporous calcium amide matrix for efficient low-temperature ammonia synthesis. *Angew. Chem. Int. Ed.* 57, 2648-2652 (2018).
11. Sato, K. *et al.* A low-crystalline ruthenium nano-layer supported on praseodymium oxide as an active catalyst for ammonia synthesis. *Chem. Sci*. 8, 674-679 (2017).
12. Ogura, Y. *et al.* Efficient ammonia synthesis over a $Ru/La_{0.5}Ce_{0.5}O_{1.75}$ catalyst pre-reduced at high temperature. *Chem. Sci.* 9, 2230-2237 (2018).
13. Hattori, M. *et al.* Enhanced catalytic ammonia synthesis with transformed BaO. *ACS Catal.* 8, 10977-10984 (2018).
14. Kitano, M. *et al*. Low-temperature synthesis of perovskite oxynitride-hydrides as ammonia synthesis catalysts. *J. Am. Chem. Soc*. 141, 20344-20353 (2019).
15. Zheng, J. *et al*. Efficient Non-dissociative Activation of Dinitrogen to Ammonia over Lithium-Promoted Ruthenium Nanoparticles at Low Pressure. *Angew. Chem. Int. Ed.* 58, 17335-17341 (2019).
16. Wu, J. *et al.* Intermetallic Electride Catalyst as a Platform for Ammonia Synthesis. *Angew. Chem. Int. Ed.* 58, 825-829 (2019).